# IMPACTS OF BUBBLES ON OPTICAL ESTIMATES OF CALCIUM CARBONATE IN THE GREAT CALCITE BELT

by

Michael Scott Brown

Submitted in partial fulfilment of the requirements
for the degree of Master of Science

at

Dalhousie University
Halifax, Nova Scotia
March 2014

*For my parents.*

# TABLE OF CONTENTS

# LIST OF TABLES

# LIST OF FIGURES

# ABSTRACT

In this MSc thesis I determine if wind-generated bubbles elevated measurements of above-water normalized water-leaving radiance ($nL_w$) and subsequent remote sensing estimates of particulate inorganic carbon (PIC) in a coccolithophore bloom on the Patagonian Shelf. Although no measurements were made of bubbles, shipboard wind speed was used as a proxy for bubble backscattering. An empirical orthogonal function (EOF) analysis was performed on $nL_w$. The first EOF accounted for 95% of the variance, and was attributed to changes in spectral amplitude. Scores of the first EOF were positively correlated with flow-through PIC backscattering ($b_b'$) $> 5 \times 10^{-4}$ m$^{-1}$, indicating that above this threshold PIC was an optically active seawater constituent. There was only evidence for a bubble elevation of $nL_w$ at values of $b_b' < 5 \times 10^{-4}$ m$^{-1}$ and wind speeds $> 12.5$ m s$^{-1}$. There was no evidence for a bubble elevation of PIC estimated using the two-band PIC algorithm.

# LIST OF ABBREVIATIONS AND SYMBOLS USED

| Abbreviation | Description |
|---|---|
| ACF | autocorrelation function |
| AOP | apparent optical property |
| AR(1) | first-order autoregressive process |
| AVHRR | Advanced Very High Resolution Radiometer |
| COG | course over ground |
| COPAS'08 | December 2008 Coccolithophores of the Patagonian Shelf expedition |
| CZCS | Coastal Zone Color Scanner |
| DMS | dimethyl sulfide |
| ECO VSF | WET Labs ECO VSF backscattering meter |
| EOF | empirical orthogonal function |
| FI | Falkland Islands |
| GCB | Great Calcite Belt |
| IOP | inherent optical property |
| LUT | lookup table |
| MetAcq | Meteorological Acquisition System |
| MicroSAS | Satlantic Micro Surface Acquisition System |
| MODIS | Moderate Resolution Imaging Spectroradiometer |
| NASA | National Aeronautics and Space Administration |
| OBPG | Ocean Biology Processing Group |
| PIC | particulate inorganic carbon |
| PS | Patagonian Shelf |
| QuikSCAT | Quick Scatterometer |
| SeaWiFS | Sea-Viewing Wide Field-of-View Sensor |
| SMI | standard mapped image |
| SOG | speed over ground |
| SO GasEx | March 2008 Southern Ocean Gas Exchange Experiment expedition |
| VIIRS | Visible Infrared Imaging Radiometer Suite |

| Symbol | Description | Units |
|---|---|---|
| $a$ | total absorption coefficient | $m^{-1}$ |
| $b_b$ | total backscattering coefficient | $m^{-1}$ |
| $b_{b,bub}$ | backscattering coefficient due to an entrained bubble population | $m^{-1}$ |
| $b_{bp}$ | backscattering coefficient due to particles | $m^{-1}$ |
| $b_{bp,acid}$ | backscattering coefficient due to particles of acidified seawater | $m^{-1}$ |
| $b_b'$ | backscattering coefficient due to PIC | $m^{-1}$ |
| $b_b*$ | average PIC-specific backscattering cross-section | $m^2\ mol^{-1}$ |
| $E_d$ | downwelling irradiance just above the sea surface | $\mu W\ cm^{-2}\ nm^{-1}$ |
| $\overline{F_0}$ | average solar irradiance | $\mu W\ cm^{-2}\ nm^{-1}$ |
| $g_1, g_2$ | fitting coefficients | $sr^{-1}$ |
| $H_s$ | significant wave height | m |
| IN, OUT, SAT | flow-through, above-water, or satellite variables, respectively | NA |
| LOW, HIGH | low or high scenarios | NA |
| $L_{sfc}$ | surface radiance | $\mu W\ cm^{-2}\ nm^{-1}\ sr^{-1}$ |
| $L_{sky}$ | sky radiance | $\mu W\ cm^{-2}\ nm^{-1}\ sr^{-1}$ |
| $L_w$ | water-leaving radiance | $\mu W\ cm^{-2}\ nm^{-1}\ sr^{-1}$ |
| MPD | median percent difference | dimensionless |
| MR | median ratio | dimensionless |
| $N_{bub}$ | number density of an entrained bubble population | $m^{-3}$ |
| $N_{bub,0}$ | number density of an entrained bubble population just below the sea surface | $m^{-3}$ |
| $n$ | sample size | dimensionless |
| $n_{eff}$ | effective sample size (adjusted for autocorrelation) | dimensionless |
| $nL_w$ | normalized water-leaving radiance | $\mu W\ cm^{-2}\ nm^{-1}\ sr^{-1}$ |
| $n_{X,Y}$ | sample size of $X$ and $Y$ | dimensionless |
| $n_{x,y}$ | sample size of $x$ and $y$ | dimensionless |

| Symbol | Description | Units |
| --- | --- | --- |
| $n_{x,y,eff}$ | effective sample size of $x$ and $y$ (adjusted for autocorrelation) | dimensionless |
| PD | absolute percent difference | dimensionless |
| $p$ | $p$-value | dimensionless |
| $p_{adj}$ | $p$-value adjusted for autocorrelation | dimensionless |
| $p_{bub}(r_{bub})$ | probability density function of an entrained bubble population at radius $r_{bub}$ | $m^{-1}$ |
| $Q_{b,bub}(r_{bub})$ | Mie backscattering efficiency factor of a single bubble of radius $r_{bub}$ | dimensionless |
| $Q_1, Q_3$ | 25th and 75th percentiles | dimensionless |
| RMSE | root-mean-square error | varies |
| $R_{rs}$ | remote sensing reflectance just above the sea surface | $sr^{-1}$ |
| $r_{bub}$ | bubble radius | m |
| $r_{OUT,IN}$ | Pearson correlation coefficient between OUT $b_b'$ and IN $b_b'$ | dimensionless |
| $r_{OUT,w}$ | Pearson correlation coefficient between OUT $b_b'$ and wind speed | dimensionless |
| $r_{rs}$ | remote sensing reflectance just below the sea surface | $sr^{-1}$ |
| $r_{r,w}$ | Pearson correlation coefficient between the residuals and wind speed | dimensionless |
| $r_{s,IN}$ | Pearson correlation coefficient between the scores and IN $b_b'$ | dimensionless |
| $r_{s,w}$ | Pearson correlation coefficient between the scores and wind speed | dimensionless |
| $r_{x,y}$ | Pearson correlation coefficient between $x$ and $y$ | dimensionless |
| $r_{x,y}'$ | Pearson correlation coefficient between $x'$ and $y'$ | dimensionless |
| $r^2$ | coefficient of determination | dimensionless |
| SIQR | semi-interquartile range | dimensionless |
| $U_{10}$ | wind speed 10 m above the sea surface | $m\ s^{-1}$ |
| $X, Y$ | theoretical vectors | dimensionless |
| $x, y$ | aligned segments of $X$ and $Y$, respectively | dimensionless |
| $x', y'$ | unaligned segments of $X$ and $Y$, respectively | dimensionless |

| Symbol | Description | Units |
| --- | --- | --- |
| $\rho$ | proportionality factor for surface reflected $L_{sky}$ | dimensionless |
| $\rho_{x,y}$ | true correlation coefficient between $x$ and $y$ | dimensionless |
| $\sigma_{x,y}$ | standard deviation of $r_{x,y}$ | dimensionless |
| $\sigma_{x,y,eff}$ | effective standard deviation of $r_{x,y}$ (adjusted for autocorrelation) | dimensionless |
| $\beta$ | volume scattering | $m^{-1}\ sr^{-1}$ |
| $\lambda$ | wavelength | nm |

# ACKNOWLEDGEMENTS

I would like to thank the following:

My family (Mom, Dad, and Kate), for their love and support.

Colette, for her love and support. And patience.

My supervisor, Dr. Jonathan Grant, for encouraging me to pursue my own research interests.

My advisory committee (Drs. William Balch, Susanne Craig, Marlon Lewis, and Christopher Taggart), for their helpful suggestions.

The Balch lab, for collecting and providing the Coccolithophores of the Patagonian Shelf (COPAS'08) dataset. Notably, Bruce Bowler patiently answered numerous questions.

Chris Jones, for his statistics expertise.

CHAPTER 1


INTRODUCTION


**1.1 A Bright Southern Ocean**


A feature characterized by bright water was identified in the Southern Ocean that completely encircles the globe from ~40°S to 60°S during austral summers (Balch et al. 2011). This feature has consistently been observed in all NASA satellite ocean color missions, which were initiated in 1978 with CZCS, and have subsequently included SeaWiFS, MODIS-Terra, MODIS-Aqua, and most recently VIIRS (Balch et al. accepted) (Figure 1.1). Bright water is indicative of elevated reflectance, i.e. the ratio of the amount of light leaving the ocean to that entering the ocean. In the context of ocean color remote sensing, reflectance is typically measured as remote sensing reflectance ($R_{rs}$; sr$^{-1}$), which is defined according to Mobley (1999):

$$R_{rs} = \frac{L_w}{E_d} \tag{1.1}$$

where $E_d$ ($\mu$W cm$^{-2}$ nm$^{-1}$) is the downwelling irradiance just above the sea surface and $L_w$ ($\mu$W cm$^{-2}$ nm$^{-1}$ sr$^{-1}$) is the water-leaving radiance, the primary radiometric quantity essential for surface ocean bio-optical studies (Hooker et al. 1999).

Reflectances, including $R_{rs}$, are classified as apparent optical properties (AOPs), which indicates that they are dependent on the medium (water and its dissolved and particulate constituents), as well as the directional structure of the ambient light field (Mobley 1994). This is in contrast to inherent optical properties (IOPs), e.g. the total absorption ($a$; m$^{-1}$) and backscattering ($b_b$; m$^{-1}$) coefficients, which are solely dependent on the medium. The AOPs and IOPs of seawater are connected through radiative transfer theory (Mobley 1994), which describes the absorption and scattering fates of photons as they travel through the water column and air-water interface. For example, $R_{rs}$ is a function of both $a$ and $b_b$. This relationship is often modeled according to Gordon et al. (1988), and is explicitly stated in Lee et al. (2002) according to:

$$r_{rs} = \sum_{i=1}^{2} g_i \left[ \frac{b_b}{a+b_b} \right]^i \tag{1.2}$$

where $r_{rs}$ (sr$^{-1}$) is $R_{rs}$ just below the sea surface, and $g_1$ and $g_2$ (sr$^{-1}$) are fitting coefficients determined by Monte Carlo simulations. Examination of Equation 1.2 indicates that $R_{rs}$ is inversely proportional to $a$, and proportional to $b_b$. Therefore, one explanation for the bright feature observed in the Southern Ocean is that it is due to the presence of backscattering seawater constituents.
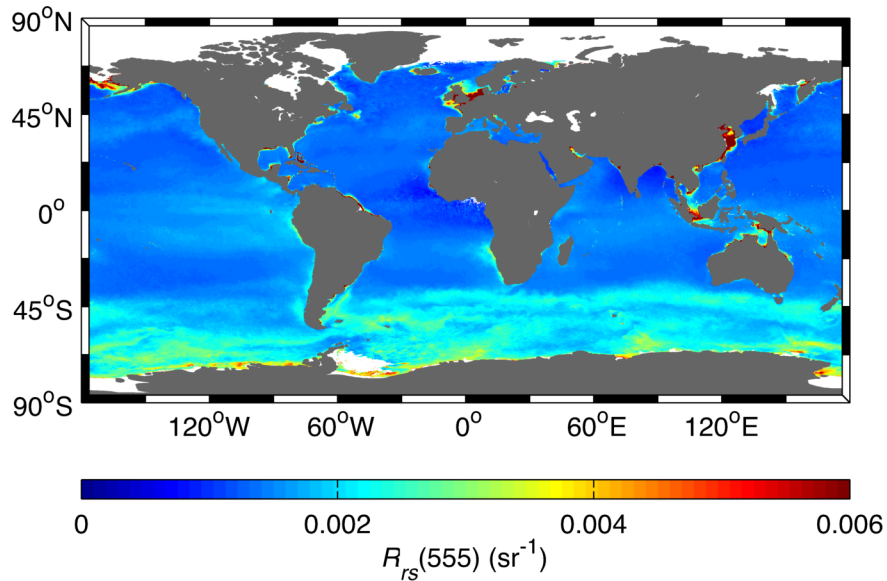


Figure 1.1. Seasonal climatology (austral summer: 21 December through 20 March) of $R_{rs}(555)$ recorded during the MODIS-Aqua mission (2002 through 2013). Note the band of elevated reflectances that encircles the globe in the Southern Ocean. Source imagery was provided by the NASA Ocean Color Web (http://oceancolor.gsfc.nasa.gov/).

**1.2 The Great Calcite Belt**

Application of particulate inorganic carbon (PIC), i.e. calcium carbonate (CaCO$_3$), remote sensing algorithms (Gordon et al. 2001, Balch et al. 2005) to the reflectances observed in the Southern Ocean yield elevated concentrations (Balch et al. 2011) (Figure 1.2). These algorithms are designed specifically to estimate calcite, a

polymorph of calcium carbonate that is produced by coccolithophores, Haptophyte algae that synthesize small (1 to 10 μm diameter) external calcite scales (coccoliths). Coccolithophores are ubiquitous throughout the global ocean (Winter et al. 1994), although blooms typically consist of the cosmopolitan species *Emiliania huxleyi* (Tyrrell and Merico 2004). During such blooms, functionally defined as cell concentrations exceeding $1 \times 10^6$ cell $L^{-1}$ (Tyrrell and Merico 2004), excess coccoliths are shed as a result of overproduction and cell senescence, typically yielding 10 to 15 detached coccoliths per cell (Paasche 2001). Coccoliths do not absorb visible light (Balch et al. 1991), but given their large size relative to visible light wavelengths, as well as the large difference between the refractive indices of calcite and water (1.58 and 1.33, respectively), they are highly efficient light scatterers. For example, coccolith backscattering can exceed 90% of total backscattering during blooms (Balch et al. 1991), and even 10% during non-bloom conditions (Balch et al. 1999). It has been demonstrated that due to the strong scattering properties of coccoliths, blooms of coccolithophores can have considerable impacts on surface ocean optics, including elevating reflectance (Holligan et al. 1983, Ackleson et al. 1988, Balch et al. 1991, Ackleson et al. 1994, Balch 1996a,b, Tyrrell et al. 1999).

Remote sensing methods used to identify coccolithophore blooms have typically exploited this strong reflectance signal. The visual characteristic of a bloom is a region of bright water with a turquoise color, and this can be observed from ships, airplanes, and even satellites. Early remote sensing methods therefore consisted of the visual identification of blooms based either on their color (Holligan et al. 1983), or just their brightness in AVHRR imagery (Groom and Holligan 1987). Such methods have become more sophisticated with the development of algorithms that automatically classify satellite imagery pixels as blooms based on their reflectance characteristics (Brown and Yoder 1994, Iglesias-Rodriguez et al. 2002, Moore et al. 2012). An alternative approach to simply identifying the spatial extent of blooms is the estimation of coccolith calcite concentration with the semianalytic two-band (Balch et al. 2005) and three-band (Gordon et al. 2001) PIC remote sensing algorithms. Both algorithms first invert reflectance to determine the backscattering coefficient due to PIC ($b_b'$; $m^{-1}$), which is then converted to PIC concentration (mol $m^{-3}$) through division by the average PIC-specific backscattering cross-section ($b_b^*$; $m^2$ $mol^{-1}$) according to:

$$PIC = \frac{b_b'}{b_b*} \tag{1.3}$$

The current estimate of $b_b*$ is 4 $m^2$ $mol^{-1}$, based on light scattering measurements of coccolithophore cultures (Balch et al. 1999).

Results from the March 2008 Southern Ocean Gas Exchange Experiment (SO GasEx) expedition provided multiple sources of evidence that the elevated reflectances observed in the Southern Ocean are at least partially due to coccolith backscattering (Balch et al. 2011). There are multiple other references to elevated coccolithophore abundance in this feature, as measured with shipboard observations, in all sectors of the Southern Ocean (summarized in Holligan et al. (2010)). As a result, this feature was named the Great Calcite Belt (GCB) (Balch et al. 2011). With a total area of ~56x$10^6$ $km^2$ (16% of the global ocean), the GCB is likely the largest water mass in the world characterized by an elevated abundance of coccolithophores (Balch et al. 2011). In addition to the optical impacts of coccolithophores, as well as their inherent ecological interest, the GCB is potentially an important feature due to the role of coccolithophores in various global biogeochemical cycles. Coccolithophores are the dominant producers of calcite on earth (Brownlee and Taylor 2004). As calcifying primary producers they contribute to the global carbon cycle through the organic carbon and carbonate pumps, which together comprise the biological pump (Rost and Riebesell 2004). These two mechanisms involve carbon fixation via photosynthesis and calcification, respectively, the products of which are exported through sinking, effectively transporting dissolved inorganic carbon from the surface ocean into the ocean interior and sediments. Photosynthesis consumes $CO_2$, and therefore the organic carbon pump can decrease the partial pressure of $CO_2$ in the surface ocean, further facilitating its absorption from the atmosphere. In contrast, and perhaps counter-intuitively, calcification produces $CO_2$ according to:

$$2HCO_3^- + Ca^{2+} \leftrightarrow CaCO_3 + H_2O + CO_2 \tag{1.4}$$
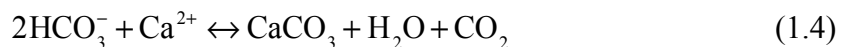
At timescales shorter than $10^3$ years the carbonate pump can increase the partial pressure of $CO_2$ in the surface ocean, facilitating its release into the atmosphere (Iglesias-Rodriguez et al. 2002). However, at timescales of $10^6$ years calcium carbonate sediments become a dominant global carbon sink (Falkowski et al. 2000). Additionally,

4

coccolithophores contribute to the global sulfur cycle through the production of dimethyl sulfide (DMS) (Malin and Steinke 2004). As a precursor of cloud condensation nuclei, DMS has important implications for planetary albedo (Charlson et al. 1987). Given its geographic size, and the role of coccolithophores in both the global carbon and sulfur cycles, the GCB is relevant to the environmental and societal issues of global climate change and ocean acidification.
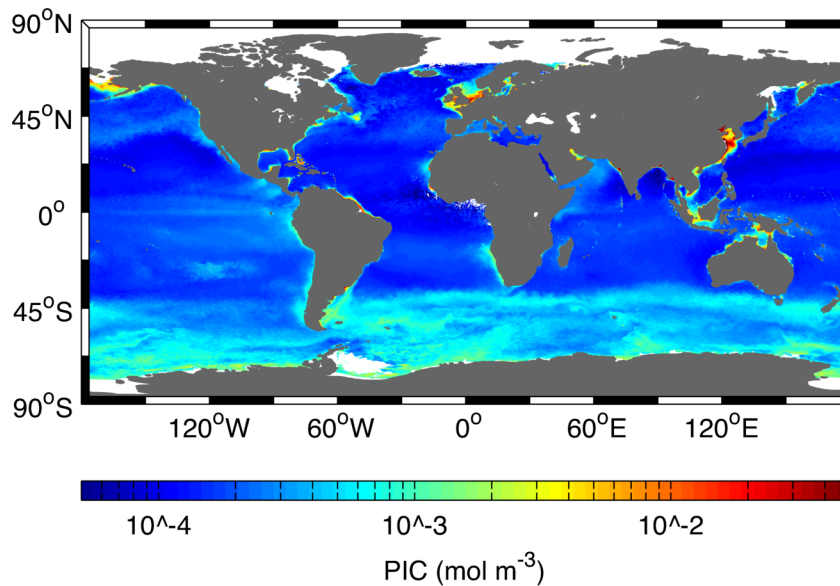


Figure 1.2. Seasonal climatology (austral summer: 21 December through 20 March) of PIC recorded during the MODIS-Aqua mission (2002 through 2013) estimated with the merged two-band/three-band algorithm (Gordon et al. 2001, Balch et al. 2005). The Great Calcite Belt can be identified as the band of elevated PIC concentrations that encircles the globe in the Southern Ocean. Source imagery was provided by the NASA Ocean Color Web (http://oceancolor.gsfc.nasa.gov/).

## 1.3 Wind-Generated Entrained Bubble Populations

Given that the Southern Ocean is characterized by strong average wind speeds (Figure 1.3), backscattering due to wind-generated entrained bubble populations could contribute to the elevated reflectances observed in the GCB. Similar to coccoliths, bubbles are highly efficient light scatterers due to their large size relative to visible light

wavelengths, as well as the large difference between the refractive indices of air and water (1.00 and 1.33, respectively). Due to continuous wind stress, waves grow, become unstable, and finally break, entraining plumes of bubbles. In the absence of precipitation, and during wind speeds exceeding 3 m s$^{-1}$, this is the dominant source of bubbles in the surface ocean (Thorpe 1992).

Monahan and Lu (1990) describe the evolution of a bubble plume immediately after entrainment. Initially confined within the top ~0.5 m, the plume subsequently expands and is mixed deeper due to turbulence. It typically reaches a depth of ~$4H_s$, where $H_s$ (m) is the significant wave height, but can extend to ~$6H_s$ (Thorpe 1995). Furthermore, the size spectrum of the plume narrows as large and small bubbles rise and dissolve, respectively. Persistent bubble radii observed in nature range from ~10 to ~300 µm (Zhang et al. 1998). However, that minimum might be due to limited instrument resolution (Zhang 2001), as smaller bubbles have been observed in the laboratory (Johnson and Cooke 1981). The remaining bubbles are immediately covered in organic films, which provide mechanical stability, and thus become "dirty" (Thorpe 1982). Additionally, as a result of dilution due to mixing, and the loss of small and large bubbles, the number density of the plume is reduced, and can range from $10^4$ to $10^8$ m$^{-3}$ (Zhang et al. 1998). Finally, during wind speeds exceeding 7 m s$^{-1}$ separate bubble plumes near the sea surface join and produce a stratus layer (Thorpe 1995). Although observations are quite variable, the number density of a wind-generated entrained bubble population ($N_{bub}$; m$^{-3}$) typically increases with wind speed, and decays exponentially with depth (Thorpe 1992). For example, Zhang (2001) modeled the number density of a bubble population at the sea surface ($N_{bub,0}$; m$^{-3}$) according to:

$$N_{bub,0} \propto U_{10}^4 \qquad (1.5)$$

where $U_{10}$ (m s$^{-1}$) is the wind speed 10 m above the sea surface, and the exponent is based on an average of values found in the literature.

Stramski (1994) conducted fundamental research on the optics of entrained bubble populations, and demonstrated with Mie scattering that bubbles could contribute a non-negligible amount of backscattering even in calm conditions. Mie scattering describes the scattering of light by a sphere, and the backscattering coefficient due to an

entrained bubble population ($b_{b,bub}$; m$^{-1}$) can be computed according to Zhang et al. (1998):

$$b_{b,bub} = \int N_{bub} Q_{b,bub}(r_{bub}) \pi r_{bub}^2 p_{bub}(r_{bub}) dr_{bub} \qquad (1.6)$$

where $Q_{b,bub}(r_{bub})$ (dimensionless) is the Mie backscattering efficiency factor of a single bubble of radius $r_{bub}$ (m), $p_{bub}(r_{bub})$ (m$^{-1}$) is the probability density function of the bubble population at radius $r_{bub}$, and the limits of the integral are the minimum and maximum radii of the bubble population. The work of Zhang et al. (1998) expanded on that of Stramski (1994), using a more representative range of bubble population spectra and number densities. They also focused on dirty bubbles, demonstrating that the backscattering efficiency of bubbles could be enhanced by a factor of four due to organic films. Using a high-resolution time series of bubble measurements, Terrill et al. (2001) showed that due to the intermittent nature of wave breaking, bubble backscattering could fluctuate dramatically over periods of minutes. Based on theory, as well as laboratory and field measurements, the volume scattering function of natural bubble populations was determined by Zhang et al. (2002). Multiple studies have demonstrated through radiative transfer modeling that bubble backscattering will elevate reflectance (Flatau et al. 2000, Stramski and Tegowski 2001, Zhang 2001, Yan et al. 2002, Zhang et al. 2004). Furthermore, although bubbles are colorless, they will have a spectral effect on reflectance, enhancing it relatively more at longer wavelengths and thus making the ocean appear greener (Zhang et al. 1998, Flatau et al. 2000, Stramski and Tegowski 2001, Zhang 2001, Zhang et al. 2004). This could potentially impact the performance of remote sensing chlorophyll algorithms that rely on ratios of blue to green light (O'Reilly et al. 1998), resulting in an overestimation. Furthermore, by elevating reflectance in the near-infrared (Zhang et al. 1998, Zhang 2001, Yan et al. 2002, Zhang et al. 2004), bubbles will cause a violation of the black pixel assumption (Siegel et al. 2000) used by standard satellite atmospheric correction procedures (Gordon and Wang 1994a).

It must be emphasized that entrained bubble populations are distinct from whitecaps at the sea surface, which also elevate reflectance (Koepke 1984, Frouin et al. 1996, Moore et al. 2000). Although both are generated by breaking waves and thus co-occur (Monahan and Lu 1990), whitecaps are not considered to be a component of $L_w$ since they surface phenomena. Therefore, an attempt is made to remove whitecaps in

standard satellite atmospheric correction procedures (Gordon and Wang 1994b) and above-water radiometric protocols (Mueller et al. 2003). I am unaware of any method that removes the scattering effects of entrained bubbles. Furthermore, while the residence time of whitecaps is seconds (Monahan and Lu 1990), entrained bubbles will typically persist for minutes (Thorpe 1995).
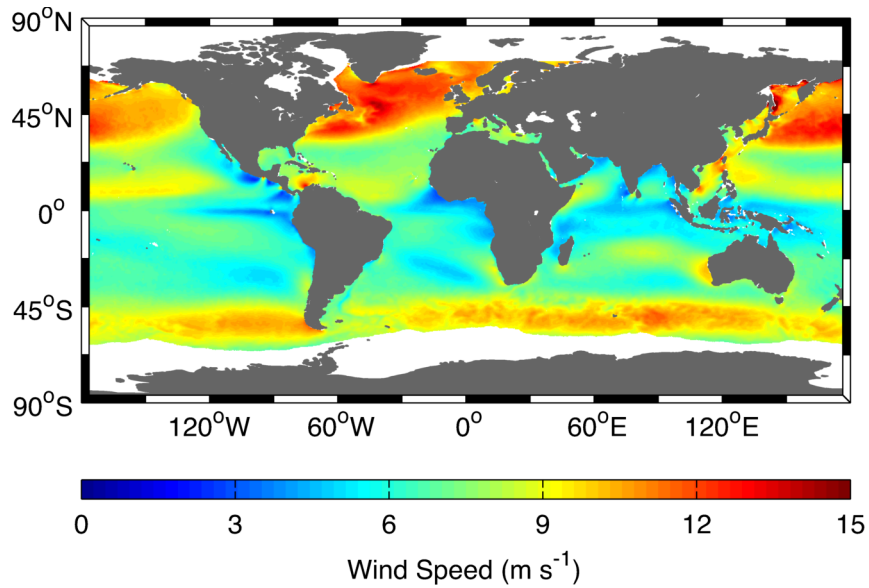


Figure 1.3. Monthly climatology (January) of wind speed recorded during the QuikSCAT mission (2000 through 2009) (Risien and Chelton 2008). Note the band of elevated wind speeds that encircles the globe in the Southern Ocean.

**1.4 Thesis Focus**

Although it has been demonstrated that backscattering due to wind-generated entrained bubble populations can impact surface ocean optics, there have been few field studies that have verified an associated elevation of $R_{rs}$ (Zhang et al. 2004, Randolph et al. 2010). However, note that Zhang et al. (2004) primarily focused on bubbles entrained by ship wakes, not wind-generated breaking waves. Furthermore, previous studies have only investigated the effects of bubbles on remote sensing chlorophyll algorithms. Regarding the semianalytic PIC algorithms (Gordon et al. 2001, Balch et al. 2005), which

rely on the magnitude of reflectance, an increase in backscattering and reflectance due to bubbles would theoretically elevate the estimated value of $b_b'$, resulting in a subsequent overestimation of PIC concentration (Equation 1.3). It is essential to determine if this phenomenon is occurring in the GCB, given its geographic size, potential biogeochemical importance, and wind field.

In this MSc thesis my goal is to determine if backscattering due to wind-generated entrained bubble populations elevated measurements of reflectance, and subsequent remote sensing estimates of PIC, using a dataset collected on the Patagonian Shelf (PS). The PS is located in the southwestern Atlantic Ocean, offshore of the Argentinean and Uruguayan coasts. It is the brightest region of the GCB (Balch et al. accepted), and is characterized by the seasonal occurrence (austral summer) of coccolithophore blooms (Brown and Podestá 1997, Signorini et al. 2006, Garcia et al. 2011). The dataset was collected during the December 2008 Coccolithophores of the Patagonian Shelf (COPAS'08) expedition, during which a mesoscale coccolithophore bloom was observed on the southern portion of the shelf (Figure 1.4). Relevant variables measured during the cruise included: 1) flow-through $b_b'$, 2) above-water normalized water-leaving radiance ($nL_w$; $\mu$W cm$^{-2}$ nm$^{-1}$ sr$^{-1}$), which is an AOP proportional to $R_{rs}$, 3) above-water $b_b'$ resulting from application of the two-band PIC algorithm (Balch et al. 2005) to the $nL_w$, and 4) shipboard wind speed. Although no measurements were made of bubbles, the shipboard wind speed was used as a proxy for $b_{b,bub}$, which is justified upon examination of Equations 1.5 and 1.6. The ultimate application of this study is to improve the ability to identify coccolithophores from remote sensing data, thereby allowing further insights into the global dynamics of this important phytoplankton group.
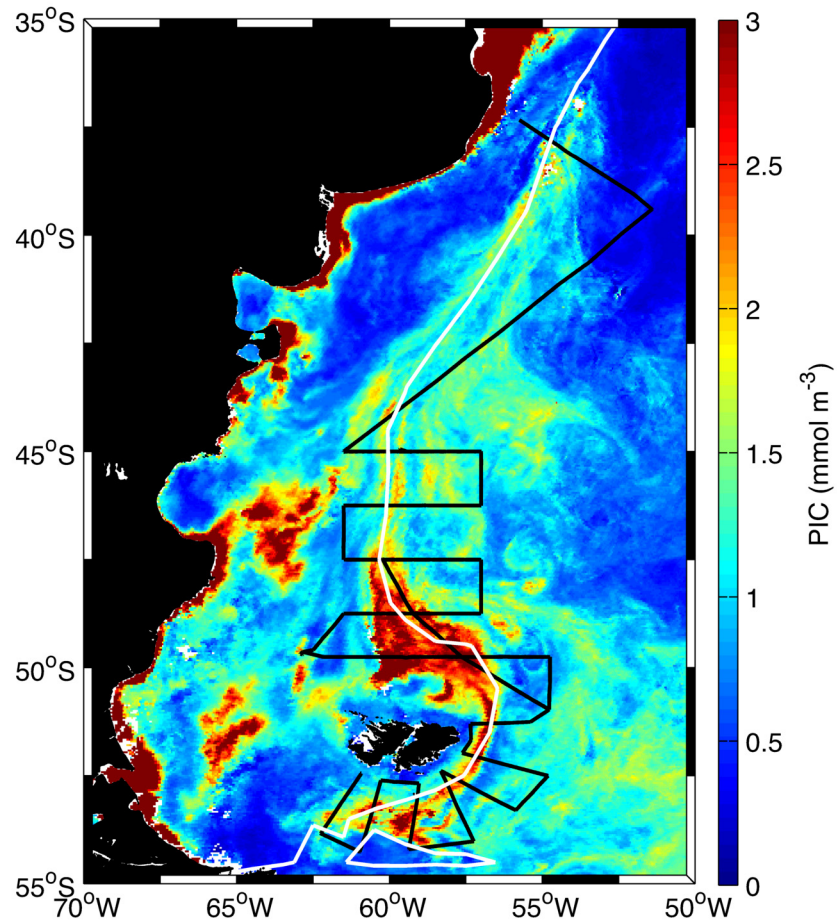
Figure 1.4. Monthly average (December 2008) of MODIS-Aqua PIC over the PS estimated with the merged two-band/three-band algorithm (Gordon et al. 2001, Balch et al. 2005). The solid black line is the COPAS'08 cruise track. The solid white line is the 1000 m bathymetry contour. Source imagery was provided by the NASA Ocean Color Web (http://oceancolor.gsfc.nasa.gov/).

CHAPTER 2


**METHODS**


**2.1 COPAS'08 Cruise Track**


The COPAS'08 cruise was conducted in the PS region onboard the R/V *Roger Revelle* (cruise "Knox 22RR") during December 2008. The ship departed Montevideo, Uruguay on 4 December 2008 and arrived in Punta Arenas, Chile on 2 January 2009. Data collection relevant to my study occurred over 27 days from 5 through 31 December 2008. Henceforth, all dates will be 2008. The cruise track (Figure 2.1) consisted of an initial southeastward transect across the shelf break, followed by a southwestward transect that crossed back onto the shelf. Between 45.0 and 50.0°S the cruise track consisted of zonal transects across the shelf break. This was followed by a northwestward transect from 51.0°S, 55.0°W to 47.5°S, 60.0°W during 21 through 23 December, with a southeastward return transect during 23 through 25 December. These two transects passed through the main axis of the portion of the coccolithophore bloom located to the north of the Falkland Islands (FI) (Figure 1.4). The cruise track then concluded with a sequence of radial transects extending away from the eastern and southern extent of the FIs.


Figure 2.1 (following page). The COPAS'08 cruise track. The circles indicate flow-through (i.e. IN) $b_b'$ measurements, and were plotted every 5th measurement for visual clarity. The data were plotted in a temporally ascending manner. Therefore, given the cruise track configuration, the northwestward transect from 51.0°S, 55.0°W to 47.5°S, 60.0°W during 21 through 23 December is covered by the southeastward return transect during 23 through 25 December. The solid black line is the COPAS'08 cruise track. The solid gray line is the 1000 m bathymetry contour.
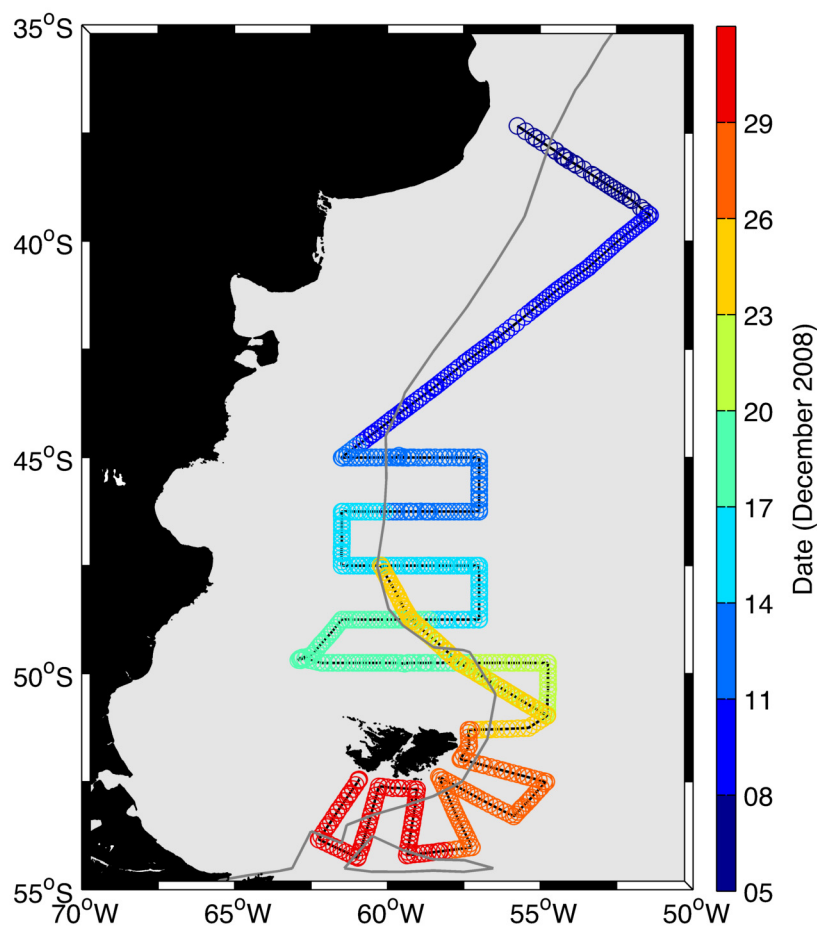
## 2.2 Flow-Through PIC Backscattering

Continuous measurements of particulate backscattering ($b_{bp}$; m$^{-1}$) were made during the cruise with a WET Labs ECO VSF backscattering meter as one part of a flow-through system located inside the ship. Balch et al. (2011) describe in detail a similar system that was used during the March 2008 SO GasEx expedition. Surface seawater was continuously collected through the ship's nontoxic sampling line, and was initially fed into a vortex debubbler before entering the flow-through system. The ECO VSF was contained in a sealed 2 L PVC chamber and measured volume scattering ($\beta$; m$^{-1}$ sr$^{-1}$) at a wavelength of 530 nm at three angles (100°, 125°, and 150°). Calculation of $b_{bp}$ was performed by first fitting a fourth-order polynomial to the three $\beta$ values and integrating

over the range of 90 to 180°, which defines the backscattering region. A Milli-Q blank was then subtracted from this result to correct for the PVC chamber wall effect and seawater backscattering, yielding $b_{bp}$.

The primary application of this flow-through system was to continuously measure $b_{bp}$ from non-acidified and acidified seawater, thereby allowing estimation of the acid-labile component of $b_{bp}$ that was due to PIC, i.e. $b_b'$. The determination of a single $b_b'$ value consisted of first making an initial sequence of $b_{bp}$ measurements. The number of measurements was typically 60, but at some points during the cruise this was adjusted to as few as 30. This was done to increase the $b_b'$ spatial and temporal resolution by reducing its measurement time. Next, any PIC present in the flow-through system seawater was dissolved by gently lowering the pH with a weak acid (10% glacial acetic acid) to < 5.8, which is below the dissociation points of calcite and aragonite. Once the pH had stabilized downstream from the ECO VSF, another sequence of $b_{bp}$ measurements was made on the acidified seawater ($b_{bp,acid}$; $m^{-1}$), equal in number to the initial non-acidified sequence. The averages of the non-acidified and acidified $b_{bp}$ measurements were then computed. Henceforth, the terms IN $b_{bp}$ and IN $b_{bp,acid}$ will refer to these averages, rather than the individual values from which they were computed. The "IN" prefix emphasizes that these variables were measured by the flow-through system ECO VSF located inside the ship, and distinguishes them from the above-water (OUT) and satellite (SAT) variables described below in the text. Finally, IN $b_b'$ was defined as the difference between IN $b_{bp}$ and IN $b_{bp,acid}$. With this procedure IN $b_b'$ was estimated every ~6 minutes during the cruise (effective spatial resolution of ~2 km assuming the median ship speed of ~5 m s$^{-1}$). This yielded 5826 IN $b_b'$ estimates.

The resulting IN $b_{bp}$, IN $b_{bp,acid}$, and IN $b_b'$ time series contained noticeably suspect values (Figure 2.2), apparent as large deviations from the surrounding data, i.e. outliers, as well as negative IN $b_b'$ values. To quality control the IN $b_b'$ time series a statistically-based flagging procedure was developed. An initial flag was designed to identify excessively short or long measurement times, which yielded data that were automatically considered suspect. A specific example of this was the initial measurement made after periods when the flow-through system was stopped for maintenance. Any record with a time differential that was not within two standard deviations of the mean

time differential was flagged and removed from all three of the time series. Another flag to identify outliers was then derived by computing a running median (11 values; ~1 h) for both the IN $b_{bp}$ and IN $b_{bp,acid}$ time series. Anomalies for both of these variables were defined as the difference between their respective time series and running median. Any record where the anomaly of either variable was not within two standard deviations of the mean anomaly was flagged. These steps were not performed for the IN $b_b'$ time series, as any large deviations that were present resulted from those in either the IN $b_{bp}$ or IN $b_{bp,acid}$ time series. An additional flag identified positive IN $b_b'$ values $< 1 \times 10^{-5}$ m$^{-1}$, which was considered to be the limit of detection. The final flag identified negative IN $b_b'$ values. While not physically meaningful, negative IN $b_b'$ values were possible given that during a 6-minute cycle the ship was moving, and therefore the flow-through system did not necessarily sample the same particle suspension during the non-acidified and acidified sequences. In total, 765 of the 5826 values (13%) were flagged and removed from the IN $b_b'$ time series. This yielded 5061 valid IN $b_b'$ estimates.
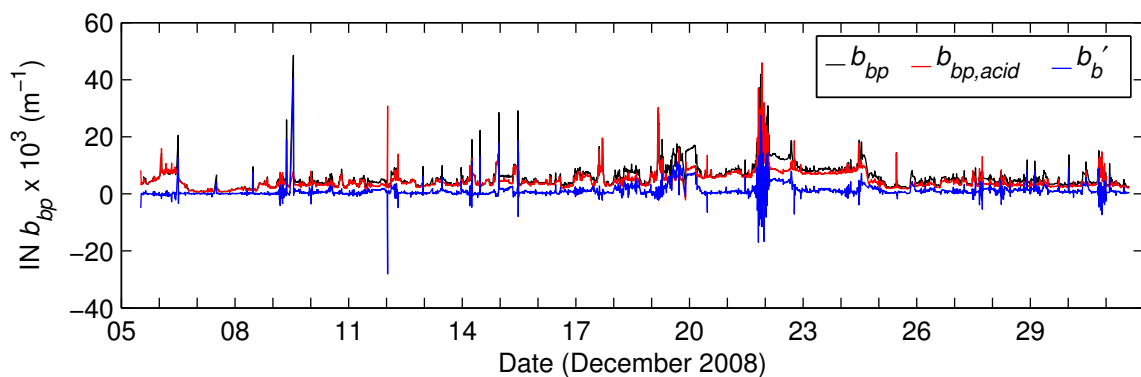


Figure 2.2. Time series of IN $b_{bp}$, IN $b_{bp,acid}$, and IN $b_b'$ before application of the flagging procedure.

## 2.3 Above-Water Radiometry

Continuous measurements of above-water radiance were made during the cruise with a Satlantic Micro Surface Acquisition System (MicroSAS). Balch et al. (2011)

describe in detail a similar system used during the March 2008 SO GasEx. The MicroSAS consisted of three radiometers (one irradiance and two radiance), all measuring at the same seven wavelengths (412, 443, 490, 510, 532, 555, and 670 nm). The irradiance radiometer was mounted at the top of the bow meteorological mast. The two radiance radiometers were mounted to the bow in such a way as to not be subject to ship shadow or reflection, and to avoid viewing bow wake.

In an above-water system, the total radiance measured by a shipboard radiometer pointed towards the sea surface ($L_{sfc}$; $\mu W$ $cm^{-2}$ $nm^{-1}$ $sr^{-1}$) is given according to Mobley (1999) and Mueller et al. (2003):

$$L_{sfc} = \rho L_{sky} + L_w \tag{2.1}$$

where $L_{sky}$ ($\mu W$ $cm^{-2}$ $nm^{-1}$ $sr^{-1}$) is the incident sky radiance and $\rho$ (dimensionless) is the proportionality factor that determines the amount of $L_{sky}$ reflected into the sea-viewing radiometer (Mobley 1999). The two MicroSAS radiance radiometers viewed the sea surface and sky to measure $L_{sfc}$ and $L_{sky}$, respectively. The radiometers were oriented 40° from nadir and zenith, respectively, and continuously viewed 120° away from the solar azimuth (Mueller et al. 2003). The latter was controlled automatically with a custom built positioning system that used navigation and time information from the ship's navigation system. Above-water radiometry was collected at 10 Hz throughout the cruise during periods when the solar zenith angle was greater than 20°. For computational storage considerations, the data were temporally averaged to ~2 s during post-processing with ProSoft (Satlantic). Using the temporally averaged $L_{sfc}$ and $L_{sky}$, $L_w$ was calculated according to Equation 2.1, with $\rho$ fixed at 0.024. Normalized water-leaving radiance ($nL_w$; $\mu W$ $cm^{-2}$ $nm^{-1}$ $sr^{-1}$), was then calculated according to Mueller et al. (2003):

$$nL_w = \frac{L_w}{E_d} \overline{F_0} \tag{2.2}$$

where $\overline{F_0}$ ($\mu W$ $cm^{-2}$ $nm^{-1}$) is the average solar irradiance (Thuillier et al. 2003). The normalization of $L_w$ to $nL_w$ is performed to account for effects of the atmosphere and solar zenith angle, and allows the comparison of $L_w$ measurements collected at different times and locations (Gordon and Clark 1981).

15

To align the temporally averaged above-water radiometry and IN $b_b'$ time series the above-water data spanning the duration of each IN $b_b'$ measurement (~6 minutes) were further temporally averaged. During this process only the lowest 5% of the above-water radiometry data in each temporal bin was accepted to eliminate the effects of whitecaps and sun glint (Mueller et al. 2003). Henceforth, the term OUT $nL_w$ will refer to these temporally averaged and quality-controlled $nL_w$ spectra. The "OUT" prefix emphasizes that this variable was measured by radiometers mounted outside on the bow of the ship, and distinguishes it from the laboratory (IN) and satellite (SAT) variables described above and below, respectively, in the text. In total, 2367 OUT $nL_w$ spectra were generated. However, 40 spectra (2%) were subsequently flagged and removed. This included 36 spectra that were incomplete and 4 that were visually identified as outliers due to their magnitude and shape. This yielded 2327 valid OUT $nL_w$ spectra. The nighttime gaps in the above-water radiometry due to the solar zenith angle restriction resulted in ~50% less OUT $nL_w$ spectra than IN $b_b'$ values (2327 versus 5061).

## 2.4 Above-Water Radiometry EOF Analysis

An empirical orthogonal function (EOF) analysis was performed on the OUT $nL_w$ spectra to identify the dominant modes of variability. Also commonly referred to as principal component analysis, EOF analysis is a multivariate statistical technique that aims to reduce the dimensionality of a dataset (Wilks 2006). Modes of variability (EOFs) within the dataset are empirically derived. These EOFs can be geometrically interpreted as vectors, or axes, in the multi-dimensional space of the dataset. The first EOF is aligned in the direction along which the dataset demonstrates the most variance. Subsequent EOFs account for progressively less variance, and are restricted to be orthogonal to the previous EOFs. New variables can be constructed by projecting the original dataset onto individual EOFs. Elements of these new variables (scores) result from linear combinations of the variables in each original dataset record weighted according to the EOF elements (loadings). By using the EOFs and scores that account for the most variance, the dimensionality of the original dataset can be reduced while retaining its primary information. EOF analysis is typically applied in the geophysical sciences to

identify spatial and temporal patterns (Wilks 2006). However, Mueller (1976) demonstrated that this technique is also useful to parameterize ocean color spectra. Recent efforts have been successful in deriving models using EOF analysis of ocean color spectra to predict bio-optical variables (e.g. Fichot et al. 2008, Craig et al. 2012, Barnes et al. 2014).

The EOF analysis was implemented on the OUT $nL_w$ spectra according to Craig et al. (2012). In this application the seven wavelengths of the spectra represented the multi-dimensional aspect of the dataset. Computation of the EOF analysis was performed with the MATLAB$^{TM}$ function *pca*, which required as input the spectra formatted into a 2327 × 7 (row × column) array, where rows corresponded to observations and columns to wavelength. It should be noted that Craig et al. (2012) ultimately used integral-normalized spectra for their study. This was done to remove any variability due to spectral amplitude, as their focus was on changes in spectral shape due to phytoplankton optical properties. However, given that spectral amplitude is of primary interest in my study, the decision was made to not normalize the spectra. The output of the EOF analysis consisted of a 7 × 7 array of the EOFs, where rows corresponded to loadings, and columns to EOF number. In addition, a 2327 × 7 array was output containing the EOF scores, where rows corresponded to observations and columns to EOF number.

## 2.5 Above-Water PIC Backscattering

The two-band PIC algorithm (Balch et al. 2005) was applied to the OUT $nL_w$ to estimate OUT $b_b'$. The algorithm requires as input $nL_w(440)$ and $nL_w(550)$, and then estimates $b_b'$ with a lookup table (LUT) (Figure 2.3). This LUT was previously generated with a forward implementation of the semianalytic model described by Gordon et al. (1988). As discussed, PIC (mol m$^{-3}$) is then estimated from $b_b'$ (m$^{-1}$) through division by $b_b^*$ (m$^2$ mol$^{-1}$) (Equation 1.3). I used a MATLAB$^{TM}$ implementation of the two-band PIC algorithm, which was constructed based on the *calcite.c* code distributed with SeaDAS 6.4. The LUT is sensor-specific, so a LUT appropriate for SeaWiFS spectra was used, which requires as input $nL_w(443)$ and $nL_w(555)$. Additionally, the LUT is constantly updated as more data become available, and the most recent version was used (created on

13 November 2013). The LUT estimates $b_b'(550)$, whereas the flow-through system ECO VSF estimated $b_b'(530)$. The spectral ($\lambda$; nm) dependence of $b_b'$ has previously been approximated as $\lambda^{-1.35}$ (Voss et al. 1998), and OUT $b_b'(550)$ was converted to OUT $b_b'(530)$ according to Gordon et al. (2001):

$$b_b'(530) = b_b'(550)\left(\frac{550}{530}\right)^{1.35} \tag{2.3}$$

Application of the two-band PIC algorithm to the 2327 OUT $nL_w$ spectra yielded 2100 OUT $b_b'$ estimates.
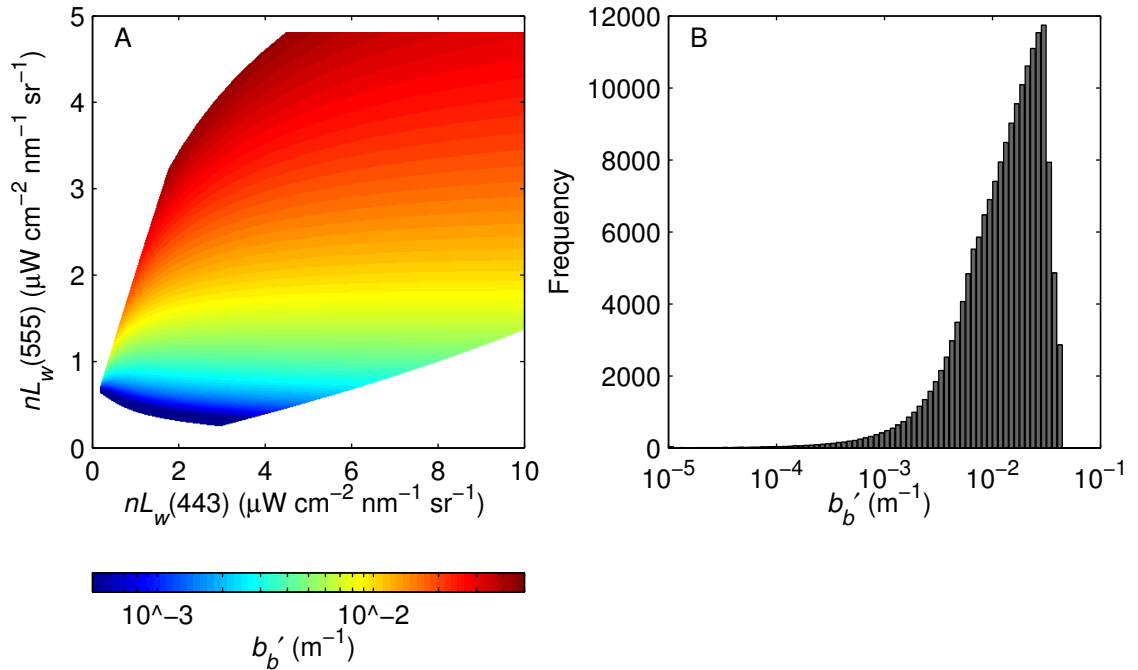


Figure 2.3. The two-band PIC algorithm SeaWiFS lookup table (LUT). A) image of the LUT, which demonstrates how the algorithm estimates $b_b'$ from measurements of $nL_w(443)$ and $nL_w(555)$ and B) histogram of the LUT $b_b'$ values.

18

**2.6 Shipboard Wind Speed**

Continuous measurements of relative wind, defined as the wind vector referenced to the ship, were made during the cruise using an ultrasonic wind sensor (Vaisala WS425A2C2B) mounted on the bow meteorological mast 17 m above the sea surface. Data were recorded every 30 s by the R/V *Roger Revelle* Shipboard Meteorological Acquisition System (MetAcq), and were merged with time, navigation, and heading information. True wind, defined as the wind vector with direction and speed referenced to true north and the fixed earth respectively, was calculated by the MetAcq using the relative wind measurements in combination with the ship's heading, course over ground (COG), and speed over ground (SOG) according to Smith et al. (1999).

To quality control the wind data, a procedure was developed based on the automatic preprocessing program described by Smith et al. (1996) to flag values that failed a series of objective tests. This procedure consisted of checking each record for the following: 1) a valid GPS fix, 2) a sequential and non-duplicate time, and 3) realistic data values. Regarding the third test, acceptable data ranges were taken from Smith et al. (1996). Variables that were verified included (acceptable data ranges in parentheses) latitude and longitude (35 to 55°S and 65 to 50°W, respectively, which were the approximate spatial bounds of the cruise track), ship heading and COG (0 to 360°), ship SOG (0 to 15 m s$^{-1}$), relative and true wind direction (0 to 360°), and relative and true wind speed (0 to 40 m s$^{-1}$). If a record failed any of the above three tests it was flagged. In total, 112 of 77759 (0.1%) records were flagged and removed. Finally, to align the quality-controlled true wind speed with the IN $b_b'$ time series the true wind speed data were temporally averaged in a manner identical to the above-water radiometry data. This yielded 5824 true wind speed measurements. Henceforth, the term "true" will be omitted with regard to wind speed for brevity.

**2.7 Satellite Radiometry**

To independently verify the above-water radiometry it was compared with corresponding satellite imagery. Global Level-3 Standard Mapped Images (SMIs) of

daily 4 km MODIS-Aqua $R_{rs}$ for all 10 available wavelengths (412, 443, 469, 488, 531, 547, 555, 645, 667, and 678 nm) were obtained for the month of December 2008 from the NASA Ocean Color Web (http://oceancolor.gsfc.nasa.gov/). The SMIs were subsetted to the region defined by the bounds 35 to 55°S and 70 to 50°W, which broadly encompasses the PS. Pixels corresponding to incomplete spectra were removed from all of the SMIs. The $R_{rs}$ was then converted to $nL_w$ according to Mueller et al. (2003):

$$nL_w = R_{rs}\overline{F_0} \qquad\qquad (2.4)$$

Henceforth, the term SAT $nL_w$ will refer to these $nL_w$ spectra. The "SAT" prefix emphasizes that this variable was measured by a satellite radiometer, and distinguishes it from the laboratory (IN) and above-water (OUT) variables described above in the text.

Comparison of the above-water and satellite radiometry was facilitated with a match-up analysis. The method for determining coincident satellite imagery was based on the NASA Ocean Biology Processing Group's (OBPG) satellite validation procedure described by Bailey and Werdell (2006). For each day of the COPAS'08 cruise, the corresponding OUT $nL_w$ records were sorted in an ascending manner according to the time differential between their measurement and 13:30 local (UTC-4), the approximate time of an ascending (daytime) MODIS-Aqua equatorial overpass. Only records within 3 h of this time were considered. For each of the sorted records, the closest pixel of the corresponding daily satellite imagery was identified. Next, a $3 \times 3$ pixel box was defined around this location. If at least 50% of the pixels encompassed were valid, then the average of the satellite imagery within the box was calculated. Finally, the valid pixels used in this calculation were then removed from consideration for subsequent match-ups. The match-up analysis yielded 81 SAT $nL_w$ spectra at various locations throughout the cruise (Figure 2.4).

It is acknowledged that the OBPG procedure avoids the use of spatially and/or temporally averaged imagery (e.g. SMIs) in satellite validation procedures (Bailey and Werdell 2006). However, the application of my match-up analysis was an independent check on the above-water radiometry, not a rigorous validation of the satellite imagery. Therefore it was determined that the use of SMIs, which are simpler to use than individual overpass imagery, was acceptable. Additionally, while the OBPG procedure defines a $5 \times 5$ satellite pixel box around *in situ* measurements, I used a $3 \times 3$ pixel box.

This was done to account for the larger spatial resolution (4 km) of the SMIs, and to ensure that fewer pixels would be removed from consideration for subsequent match-ups. Finally, the presence of outliers within each box was not diagnosed. This was justified because SMIs are the result of spatially and temporally averaged imagery that has already been quality controlled.
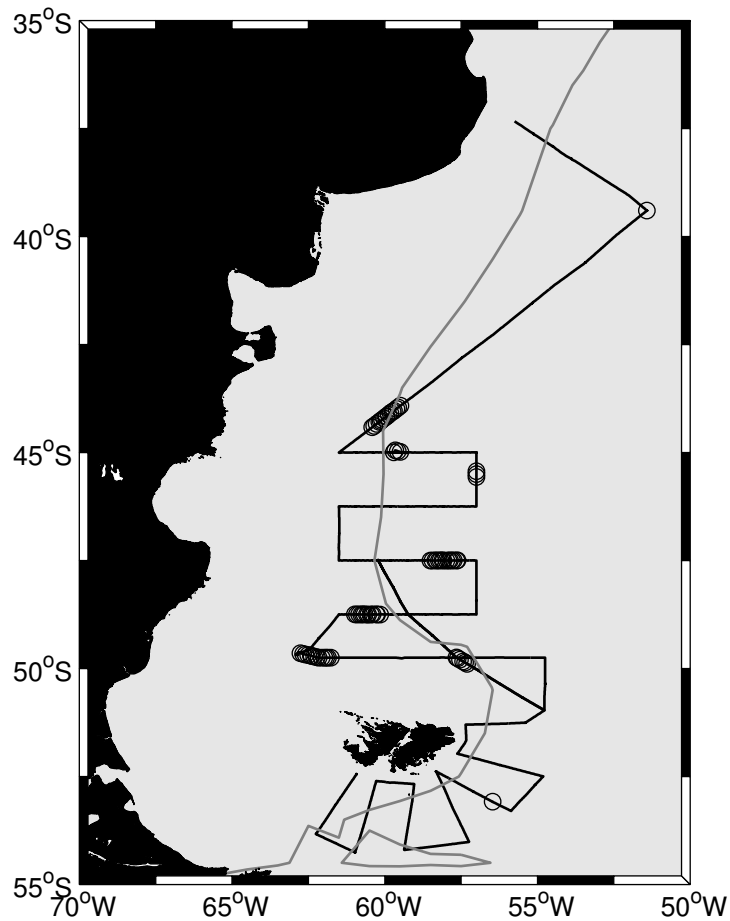


Figure 2.4. Locations of the OUT $nL_w$ and SAT $nL_w$ match-ups. The solid black line is the COPAS'08 cruise track. The solid gray line is the 1000 m bathymetry contour.

CHAPTER 3

RESULTS

**3.1 Flow-Through PIC Backscattering**

IN $b_b'$ spanned four orders of magnitude from $10^{-5}$ to $10^{-2}$ m$^{-1}$, although the data were concentrated within a range of $10^{-4}$ to $10^{-3}$ m$^{-1}$ (Figure 3.1A). The dominant signal in the time series was a sequence of three periods of consistently elevated values during 19 through 20, 21 through 22, and 24 through 25 December (Figure 3.2A). These periods correspond to three transects through the center of the coccolithophore bloom located to the northeast of the FIs at 50°S, 57.5°W (Figures 1.4 and 3.3A). The highest values of the cruise were seen in this area, with maximum values of ~11x10$^{-3}$, 8x10$^{-3}$, and 5x10$^{-3}$ m$^{-1}$ during the three transects, respectively. Elevated values (~3x10$^{-3}$) were also seen in the portion of the bloom encircling the FIs to the east and south, to the northwest of the FIs, and to a lesser extent as far north of the FIs as 42.5°S (Figure 3.3A).
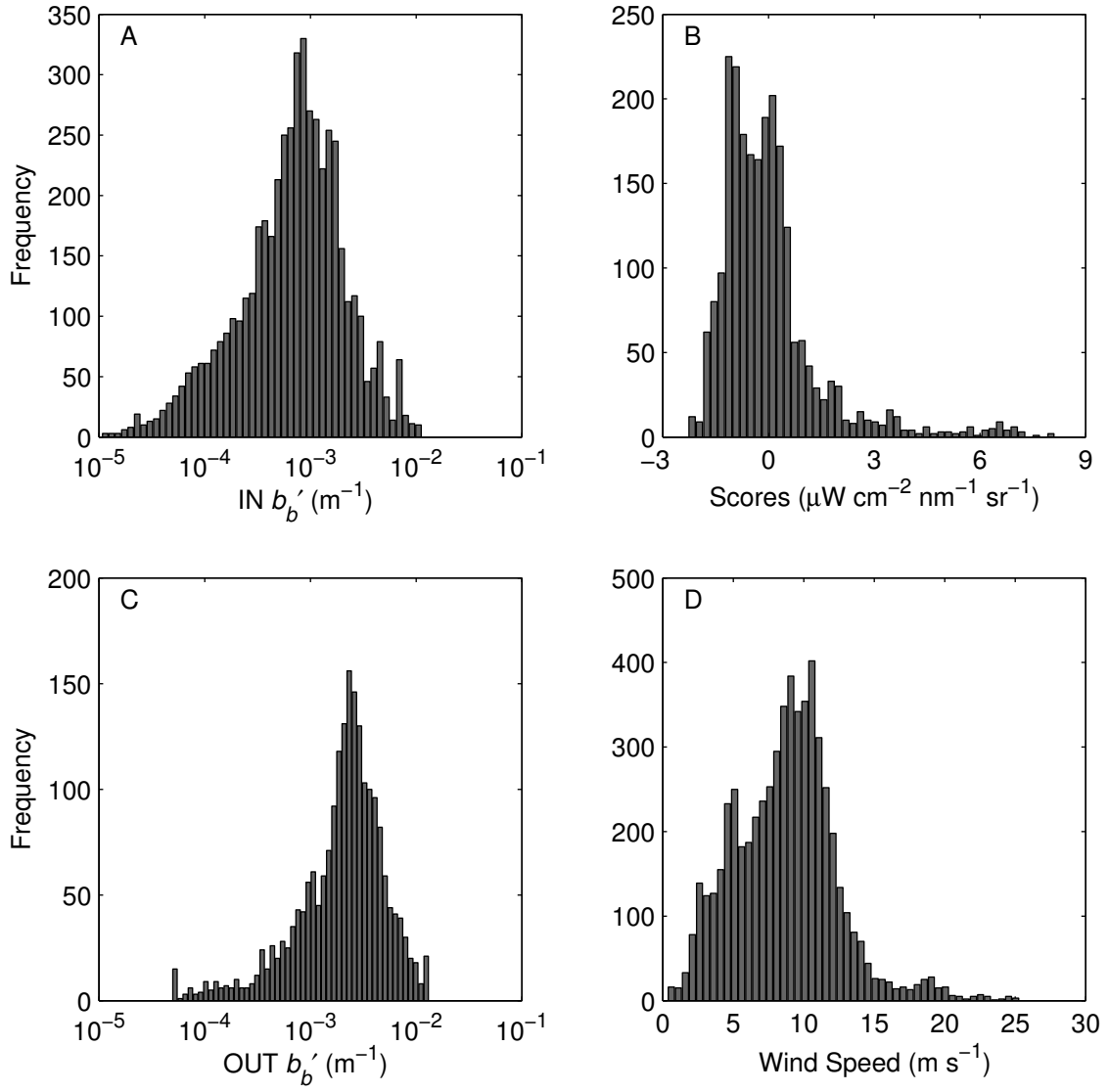
Figure 3.1. Histograms of A) IN $b_b'$, B) scores of the first OUT $nL_w$ EOF, C) OUT $b_b'$, and D) wind speed. The x-axes of panels A and C are shown on a logarithmic scale as IN $b_b'$ and OUT $b_b'$ spanned multiple orders of magnitude.
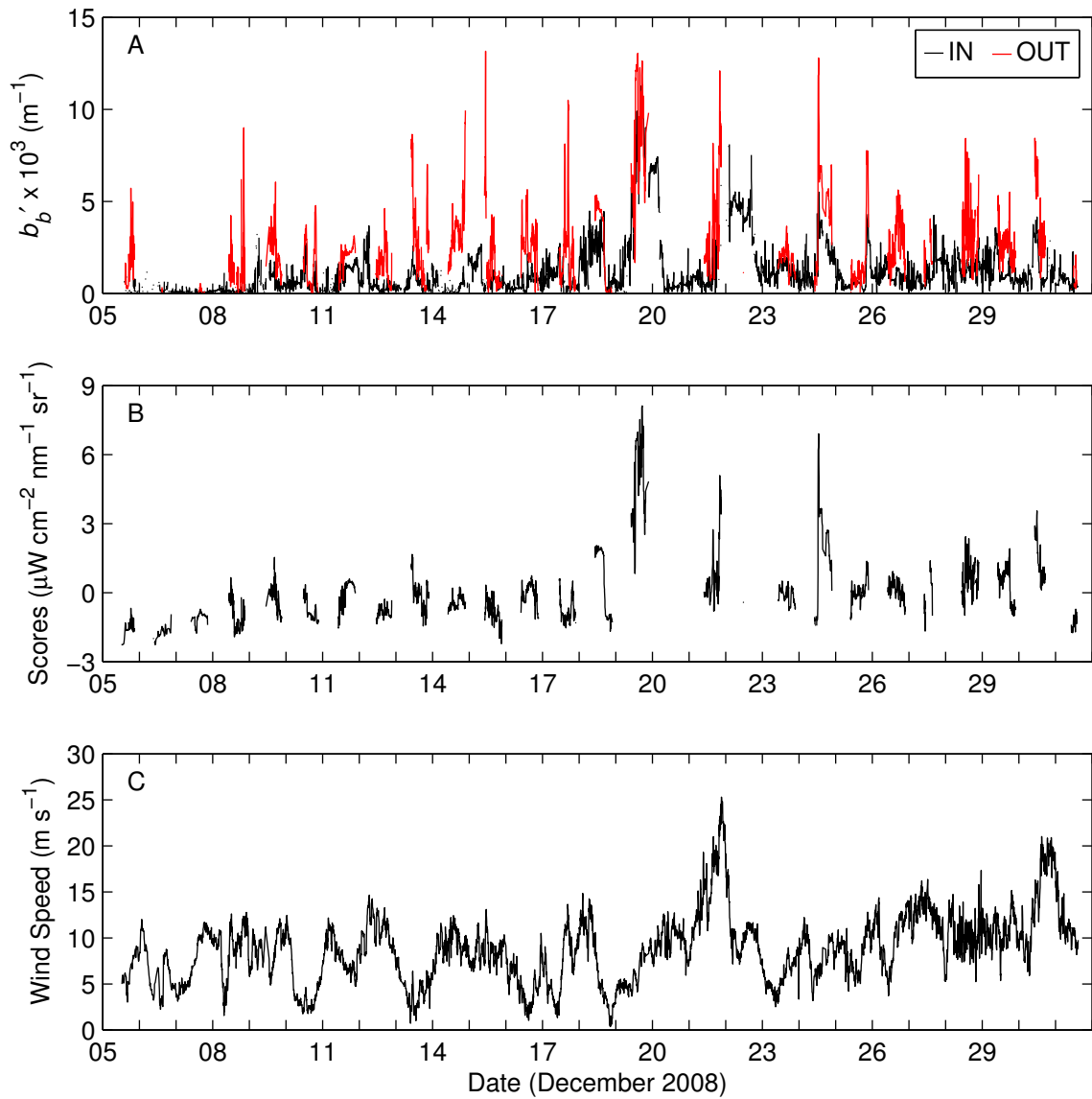
Figure 3.2. Time series of A) IN $b_b'$ and OUT $b_b'$, B) scores of the first OUT $nL_w$ EOF, and C) wind speed. The gaps in the scores and OUT $b_b'$ occurred at night, and were due to the solar zenith angle restriction on the above-water radiometry.

24
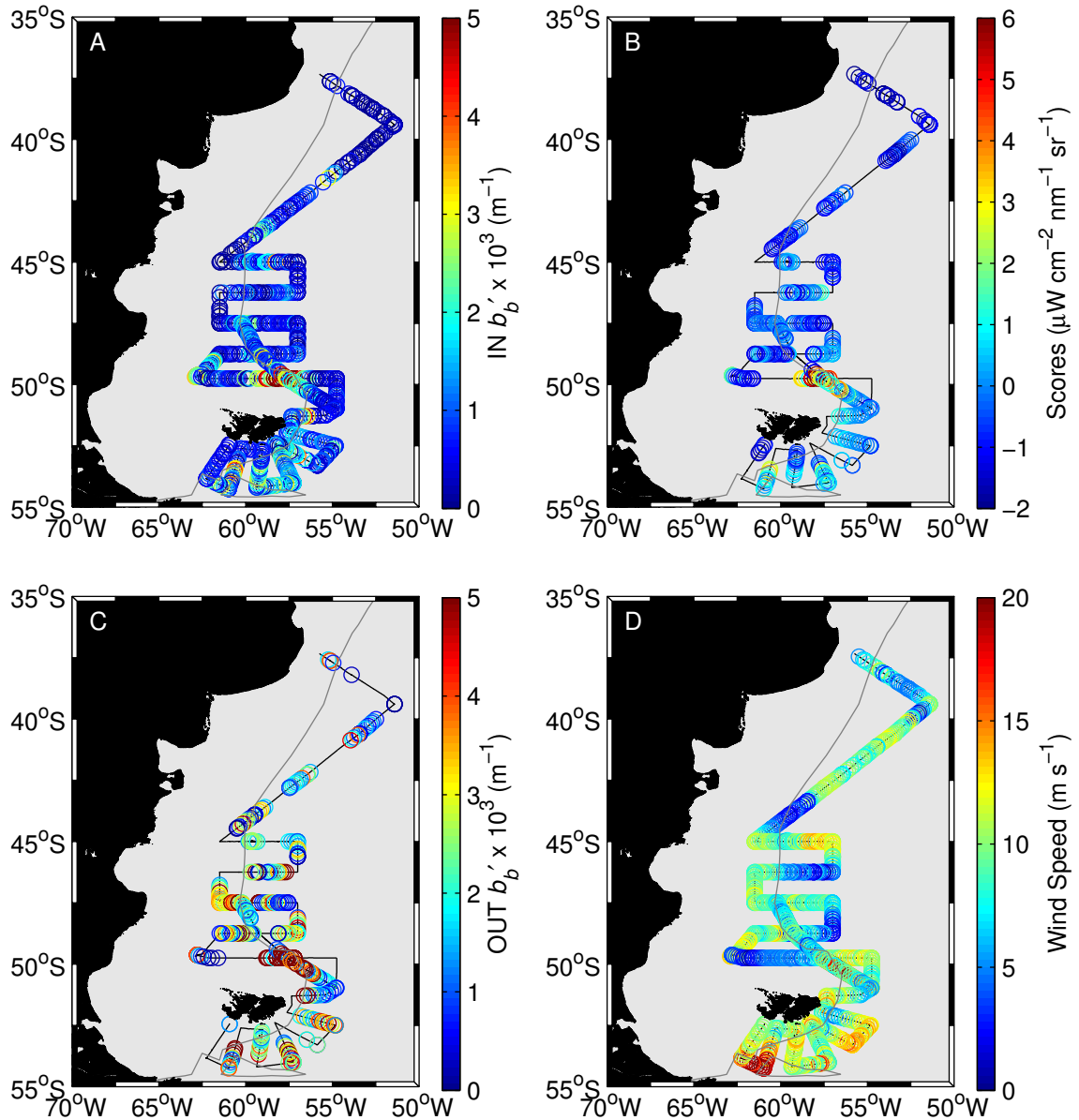
Figure 3.3. Surface plots of A) IN $b_b'$, B) scores of the first OUT $nL_w$ EOF, C) OUT $b_b'$, and D) wind speed. Data were plotted every five measurements for visual clarity. Data were plotted in a temporally ascending manner, and therefore some sections are self-covered (refer to Figure 2.1 for details). The gaps in the scores and OUT $b_b'$ occurred at night, and were due to the solar zenith angle restriction on the above-water radiometry. The solid black lines are the COPAS'08 cruise track. The solid gray lines are the 1000 m bathymetry contour.

## 3.2 Above-Water Radiometry

The dominant shape of the OUT $nL_w$ spectra was characterized by an increase with wavelength from 412 nm to a maximum at 490 nm in the blue region of the spectrum, followed by a decrease with wavelength to a minimum at 670 nm (Figure 3.4A). The spectra demonstrated the most variability at lower wavelengths, for example $nL_w$(412) and $nL_w$(670) were primarily within 3.0 and 1.0 $\mu$W cm$^{-2}$ nm$^{-1}$ sr$^{-1}$, respectively. Spectra with elevated amplitudes were clearly associated with higher IN $b_b'$ values. When the spectra were normalized by their integral to emphasize variations in shape rather than amplitude, a secondary shape was evident (Figure 3.4B). This shape was characterized by a maximum at either 532 or 555 nm in the green region of the spectrum, and was associated with lower IN $b_b'$ values.
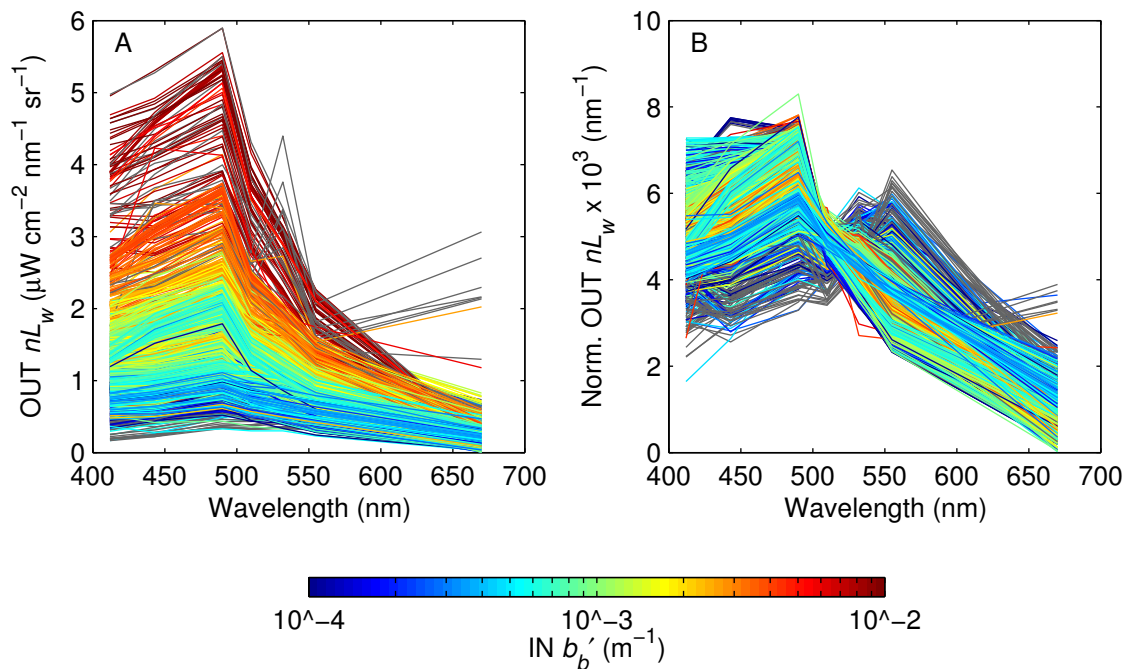


Figure 3.4. OUT $nL_w$ spectra. A) non-normalized and B) integral-normalized. Spectra are colored according to the coincident IN $b_b'$ values, where gray indicates missing values.

26

### 3.3 Above-Water Radiometry EOF Analysis

The first OUT $nL_w$ EOF represented the primary mode of variability, as it accounted for 95% of the variance in the dataset (Figure 3.5A). The shape of the first EOF, visualized by plotting its loadings versus wavelength (Figure 3.5B), resembled the dominant shape of the OUT $nL_w$ spectra (Figure 3.4A). Additionally, all the loadings were of the same sign, indicating that this mode of variability affected the entire spectrum in the same manner. Therefore, the first EOF was attributed to changes in the amplitude of the OUT $nL_w$ spectra. This mode of spectral variability is of primary interest, as it is theoretically dependent on seawater backscattering constituents such as PIC and bubbles (Equation 1.2). As a result, I decided to use the scores of the first EOF (henceforth simply "scores") as a surrogate for the OUT $nL_w$ spectra. To reiterate, each score was a single value that resulted from projecting an individual OUT $nL_w$ spectrum onto the mode of variability defined by the first EOF. This reduced the dimensionality of the OUT $nL_w$ dataset from seven to one while retaining 95% of its information. Therefore, the scores provided a parsimonious means of representing the OUT $nL_w$ spectra.

The scores ranged from -2 to 8 $\mu$W cm$^{-2}$ nm$^{-1}$ sr$^{-1}$, although they were primarily < 3 $\mu$W cm$^{-2}$ nm$^{-1}$ sr$^{-1}$ (Figure 3.1B). As with IN $b_b'$, the highest values of the cruise were seen during the three transects through the center of the coccolithophore bloom located to the northeast of the FIs, with maximum values of 8, 5, and 7 $\mu$W cm$^{-2}$ nm$^{-1}$ sr$^{-1}$, respectively (Figures 3.2B and 3.3B). In general, elevated scores were observed in regions of elevated IN $b_b'$, including the portion of the bloom encircling the FIs to the east and south, to the northwest of the FIs, and as far north of the FIs as 42.5°S (Figure 3.3A and B).
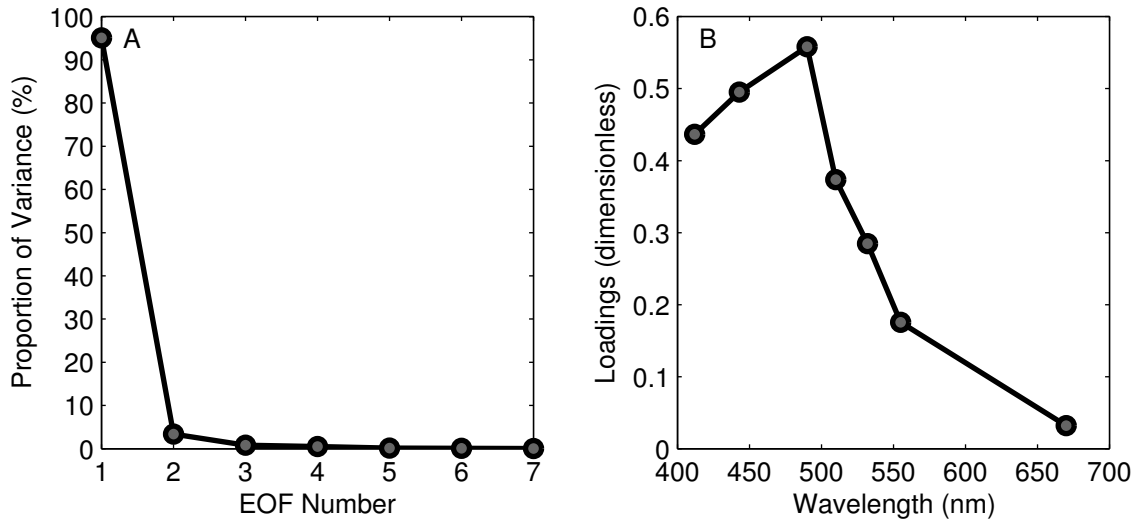
Figure 3.5. A) scree plot demonstrating the proportion of the OUT $nL_w$ variance explained by each EOF and B) loadings of the first EOF versus wavelength.

## 3.4 Above-Water PIC Backscattering

OUT $b_b'$ spanned four orders of magnitude from $10^{-5}$ to $10^{-2}$ m$^{-1}$ (Figure 3.1C), similar to IN $b_b'$ (Figure 3.1A). However, OUT $b_b'$ was concentrated within $10^{-3}$ to $10^{-2}$ m$^{-1}$, at the upper end of this range. Some of the highest values of OUT $b_b'$ were seen during the three transects through the center of the coccolithophore bloom located to the northeast of the FIs, with a typical maximum value of $\sim 1 \times 10^{-2}$ (Figures 3.2A and 3.3C). In general, OUT $b_b'$ was elevated relative to IN $b_b'$, and the two variables did not consistently covary (Figures 3.2A and 3.3A and C).

## 3.5 Shipboard Wind Speed

Wind speed ranged from 0 to 25 m s$^{-1}$, although it was primarily < 15 m s$^{-1}$ (Figure 3.1D). The cruise encountered two periods of strong wind. The first occurred during 21 through 22 December, coinciding with the second transect through the center of the coccolithophore bloom located to the northeast of the FIs (Figures 3.2C and 3.3D). The second occurred during 30 through 31 December, when the ship was located to the

southwest of the FIs. During these two periods the maximum wind speed observed was ~25 and 21 m s$^{-1}$, respectively.

## 3.6 Satellite and Above-Water Radiometry Comparison

Similar to the OUT $nL_w$ spectra, the dominant shape of the SAT $nL_w$ spectra was characterized by a maximum around 490 nm in the blue region of the spectrum, followed by a minimum at longer wavelengths (Figure 3.6A). As before, the spectra demonstrated the most variability at lower wavelengths, and those with elevated amplitudes were clearly associated with higher values of IN $b_b'$. A secondary shape was again identified in the integral-normalized spectra, which was characterized by a maximum around 555 nm in the green region of the spectrum and associated with lower values of IN $b_b'$ (Figure 3.6B).

The magnitude of OUT $nL_w$ and SAT $nL_w$ was compared at their common wavelengths (412, 443, 490/488, 532/531, 555, and 670/667 nm; OUT/SAT) with statistical metrics used by Bailey and Werdell (2006). For each wavelength, the ratio and absolute percent difference (PD; dimensionless) between coincident SAT and OUT values were computed according to the following expressions:

$$\text{Ratio}_i = \frac{\text{SAT}_i}{\text{OUT}_i} \tag{3.1}$$

$$\text{PD}_i = \frac{\left|\text{SAT}_i - \text{OUT}_i\right|}{\text{OUT}_i} \times 100 \tag{3.2}$$

where $i$ indicates the $i$th match-up. The median ratio (MR; dimensionless) and median percent difference (MPD; dimensionless) were then computed. The semi-interquartile range (SIQR; dimensionless) of the ratios was also determined according to the following expression:

$$\text{SIQR} = \frac{Q_3 - Q_1}{2} \tag{3.3}$$

where $Q_1$ and $Q_3$ (dimensionless) are the 25th and 75th percentiles, respectively. Additionally, for each wavelength SAT $nL_w$ was regressed onto OUT $nL_w$, and the slope,

coefficient of determination ($r^2$; dimensionless), and root-mean-square error (RMSE) of the resulting least-squares regression line was computed.

The results of this analysis are shown in Figure 3.7 and summarized in Table 3.1. There was general agreement between the magnitude of OUT $nL_w$ and SAT $nL_w$. The only exception was the comparison of OUT $nL_w(670)$ and SAT $nL_w(667)$, but this was attributed to incorrect atmospheric correction of the satellite imagery due to violation of the black pixel assumption, and those results were not considered. For the other wavelengths the MR was primarily within 20% of unity, with a typical SIQR of ~0.070. A negative bias in the satellite data was evident given that the MR was consistently less than unity. The MPD ranged from 15.18 to 22.32%. There was a systematic decrease in the regression slopes with wavelength, and the furthest deviation of the slope from unity was 0.624. Finally, the $r^2$ was generally greater than 0.750, and the typical RMSE was ~0.150 $\mu$W cm$^{-2}$ nm$^{-1}$ sr$^{-1}$.

Table 3.1. OUT $nL_w$ and SAT $nL_w$ comparison statistics. Here $n$ (dimensionless) is the sample size.

| OUT Wavelength[a] | MR ($\pm$ SIQR) | MPD | Slope | $r^2$ | RMSE[b] | $n$ |
|---|---|---|---|---|---|---|
| 412 | 0.813 ($\pm$ 0.086) | 20.27 | 0.898 | 0.817 | 0.169 | 73 |
| 443 | 0.837 ($\pm$ 0.075) | 18.62 | 0.851 | 0.809 | 0.180 | 73 |
| 490[c] | 0.782 ($\pm$ 0.070) | 22.32 | 0.805 | 0.833 | 0.182 | 73 |
| 532[d] | 0.854 ($\pm$ 0.066) | 15.18 | 0.741 | 0.752 | 0.113 | 73 |
| 555 | 0.822 ($\pm$ 0.067) | 17.84 | 0.624 | 0.742 | 0.089 | 73 |
| 670[e] | 0.627 ($\pm$ 0.131) | 38.12 | 0.219 | 0.329 | 0.028 | 73 |

[a]Units: nm [b]Units: $\mu$W cm$^{-2}$ nm$^{-1}$ sr$^{-1}$
[c]SAT $nL_w(488)$ [d]SAT $nL_w(531)$ [e]SAT $nL_w(667)$
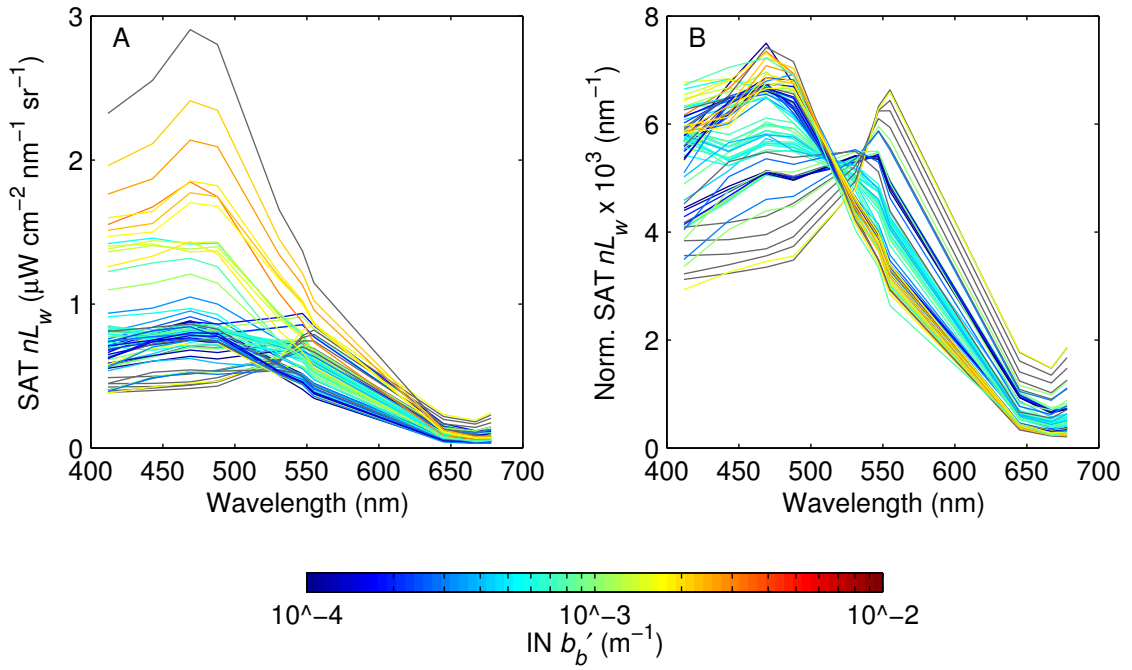
Figure 3.6. SAT $nL_w$ spectra. A) non-normalized and B) integral-normalized. Spectra are colored according to the coincident IN $b_b'$ values, where gray indicates missing values.
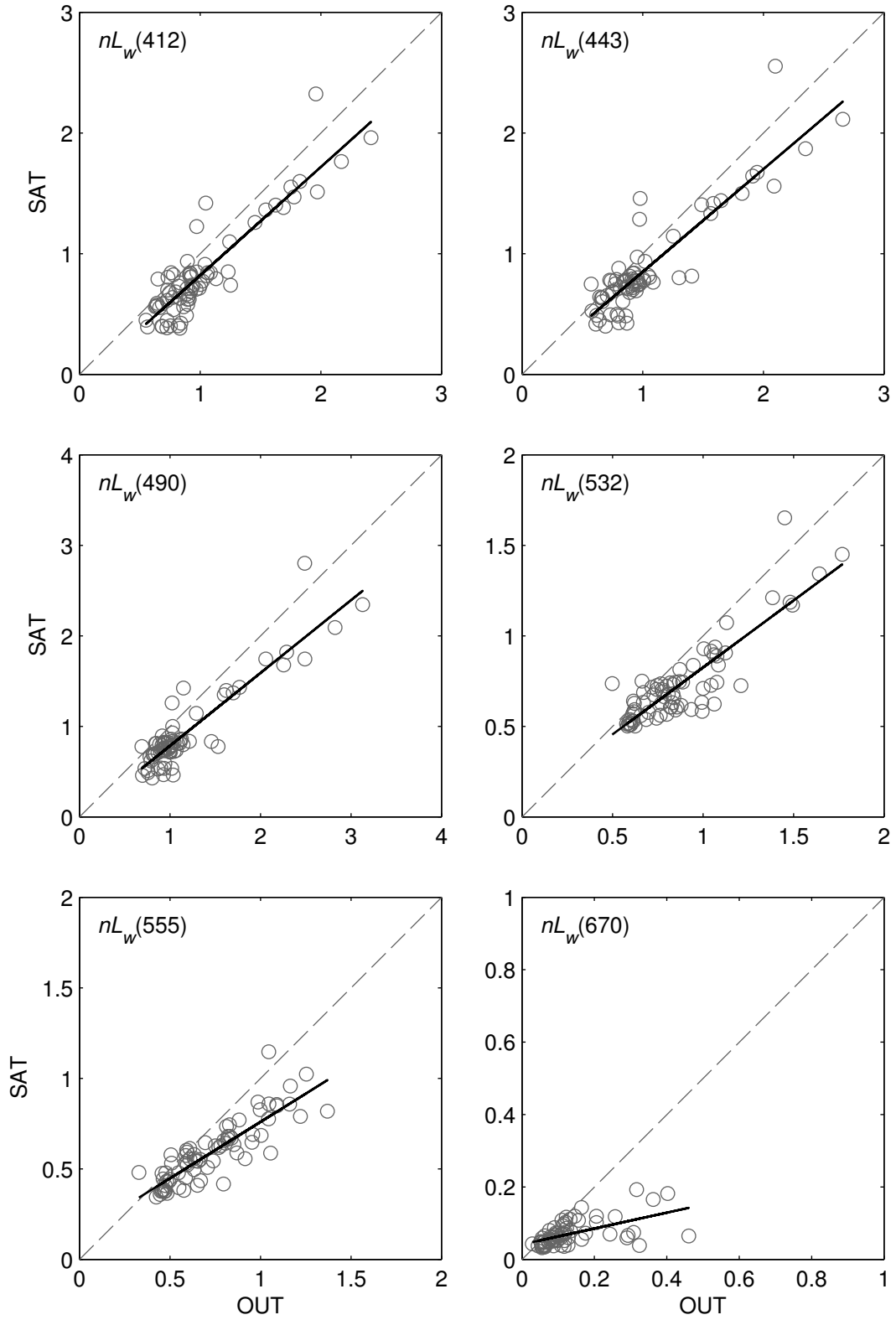
Figure 3.7. SAT $nL_w$ versus OUT $nL_w$. The solid black lines are the least-squares regression lines. The dashed gray lines are the 1:1 lines. All units are µW cm$^{-2}$ nm$^{-1}$ sr$^{-1}$.

32

## 3.7 Wind Speed Elevation of Above-Water Radiometry

A positive correlation between the scores and wind speed would have suggested an elevation of OUT $nL_w$ due to wind speed, and therefore entrained bubbles. However, there was no clear relationship between the scores and wind speed (Figure 3.8A). For a given wind speed, increasing scores were generally associated with increasing IN $b_b'$, as indicated by the horizontal bands of color. A positive correlation was possibly apparent between the scores and wind speed approximately $> 12.5$ m s$^{-1}$. However, it was not clear if this relationship was apparent only because of a relative lack of observations in the dataset that occurred during high wind speeds, particularly in combination with low values of IN $b_b'$. In contrast, a clear positive correlation was apparent between the scores and IN $b_b'$, although this relationship existed primarily at IN $b_b'$ approximately $> 5 \times 10^{-4}$ m$^{-1}$ (Figure 3.8B). For a given value of IN $b_b'$, increasing scores were not associated with increasing wind speed, as indicated by the absence of horizontal bands of color.

It was considered that the strong relationship between the scores and IN $b_b'$ might have obfuscated a comparatively minor relationship between the scores and wind speed. It was also considered that these relationships might have varied depending on the magnitude of IN $b_b'$ and wind speed. To investigate this, the dataset was isolated into four different combinations of low and high IN $b_b'$ and wind speed. This was accomplished by first isolating the dataset into LOW and HIGH IN $b_b'$ scenarios. A threshold of $5 \times 10^{-4}$ m$^{-1}$ was used, as above this value the scores displayed a positive correlation with IN $b_b'$ (Figure 3.8B). The two resulting IN $b_b'$ scenarios were then further isolated into LOW and HIGH wind speed scenarios. A threshold of $12.5$ m s$^{-1}$ was used, as above this value a positive correlation between the scores and wind speed was possibly apparent (Figure 3.8A).

The following steps were then performed for each of these four scenarios. First, the Pearson correlation coefficient was computed between the scores and IN $b_b'$ ($r_{s,IN}$; dimensionless). Statistical significance was defined at $\alpha = 0.05$, and was based on $p_{adj}$ (dimensionless), a $p$-value adjusted for any autocorrelation present in the data (Appendix A). If $r_{s,IN}$ was significant, a least-squares linear regression model was constructed using

IN $b_b'$ and the scores as predictor and response variables, respectively. The residuals of this model represented the unexplained variability in the scores. The correlation coefficient was then computed between the residuals and wind speed ($r_{r,w}$; dimensionless) to examine a potential effect of wind speed on the scores. However, if $r_{s,IN}$ was not significant, the correlation coefficient was computed between the scores and wind speed ($r_{s,w}$; dimensionless) to examine a potential effect of wind speed on the scores. A positive value of either $r_{r,w}$ or $r_{s,w}$ would have suggested an elevation of the scores (and therefore OUT $nL_w$) due to wind speed (and therefore entrained bubbles).

The results of this analysis are shown in Figures 3.9 and 3.10, and the corresponding statistics are summarized in Tables 3.2 and 3.3. Three primary observations were apparent: 1) the correlation between the scores and IN $b_b'$ was only significant in the two HIGH IN $b_b'$ scenarios (LOW wind speed: $r_{s,IN}$ = 0.867, HIGH wind speed: $r_{s,IN}$ = 0.705; Table 3.2, Figures 3.9A and C and 3.10A and C), 2) the correlation between the residuals and wind speed was not significant in either of the HIGH IN $b_b'$ scenarios (Table 3.3, Figure 3.10B and D), and 3) the correlation between the scores and wind speed was only significant in the LOW IN $b_b'$, HIGH wind speed scenario ($r_{s,w}$ = 0.755; Table 3.3, Figure 3.9B and D). Therefore, the scores were only correlated with IN $b_b'$ at values of IN $b_b'$ > $5\times10^{-4}$ m$^{-1}$, and there was only an elevation of the scores due to wind speed at wind speeds > 12.5 m s$^{-1}$ in combination with values of IN $b_b'$ < $5\times10^{-4}$ m$^{-1}$.

Table 3.2. Pearson correlation coefficients between the scores and IN $b_b'$ ($r_{s,IN}$) for the four scenarios of LOW and HIGH IN $b_b'$ and wind speed. Here $n_{eff}$ and $p_{adj}$ are the sample size ($n$; dimensionless) and $p$-value ($p$; dimensionless), respectively, adjusted for any autocorrelation present in the data (Appendix A). Bolded correlations are significant at $\alpha$ = 0.05 based on $p_{adj}$.

| IN $b_b'$ | Wind Speed | $r_{s,IN}$ | $n$ | $p$ | $n_{eff}$ | $p_{adj}$ |
|---|---|---|---|---|---|---|
| LOW | LOW | 0.223 | 680 | < 0.001 | 24 | 0.271 |
| LOW | HIGH | -0.103 | 52 | 0.468 | 13 | 0.678 |
| HIGH | LOW | **0.867** | **1206** | **< 0.001** | **42** | **< 0.001** |
| HIGH | HIGH | **0.705** | **138** | **< 0.001** | **13** | **0.013** |

Table 3.3. Pearson correlation coefficients between the residuals and wind speed ($r_{r,w}$) or the scores and wind speed ($r_{s,w}$) for the four scenarios of LOW and HIGH IN $b_b'$ and wind speed. Here $n_{eff}$ and $p_{adj}$ are the sample size ($n$; dimensionless) and $p$-value ($p$; dimensionless), respectively, adjusted for any autocorrelation present in the data (Appendix A). Bolded correlations are significant at $\alpha$ = 0.05 based on $p_{adj}$.

| IN $b_b'$ | Wind Speed | $r_{r,w}$ | $r_{s,w}$ | $n$ | $p$ | $n_{eff}$ | $p_{adj}$ |
|---|---|---|---|---|---|---|---|
| LOW | LOW | - | 0.088 | 680 | 0.022 | 17 | 0.719 |
| LOW | HIGH | - | **0.755** | **52** | **< 0.001** | **8** | **0.020** |
| HIGH | LOW | 0.035 | - | 1206 | 0.230 | 29 | 0.844 |
| HIGH | HIGH | 0.267 | - | 138 | 0.002 | 8 | 0.456 |
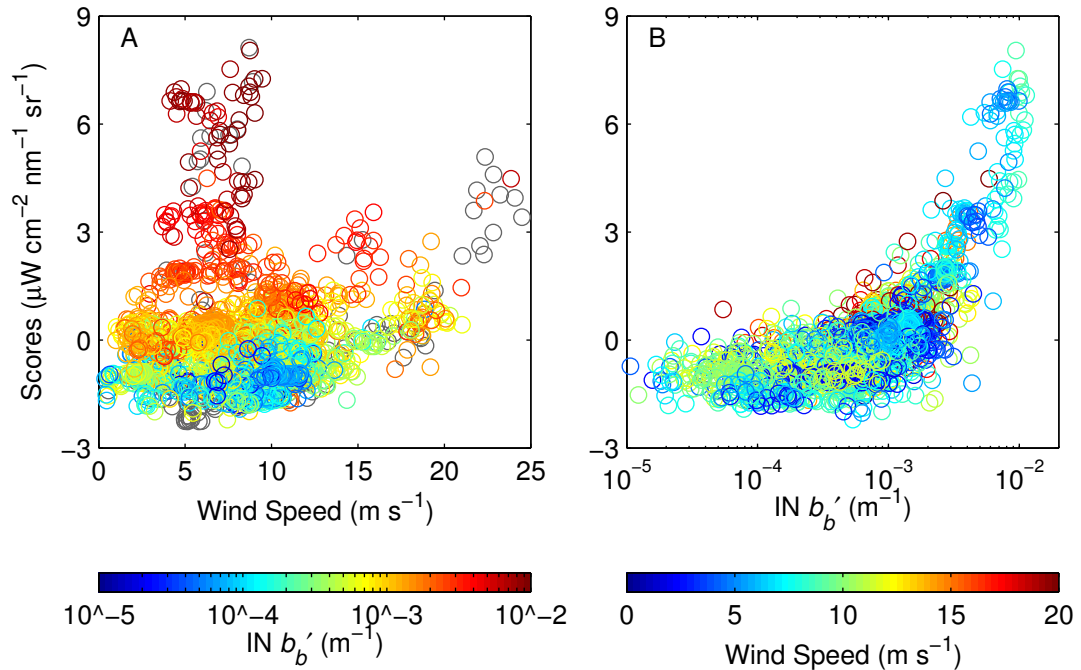
Figure 3.8. Scores of the first OUT $nL_w$ EOF versus A) wind speed and B) IN $b_b'$. Data points in panels A and B are colored according to the coincident IN $b_b'$ values and wind speeds, respectively, where gray indicates missing values.
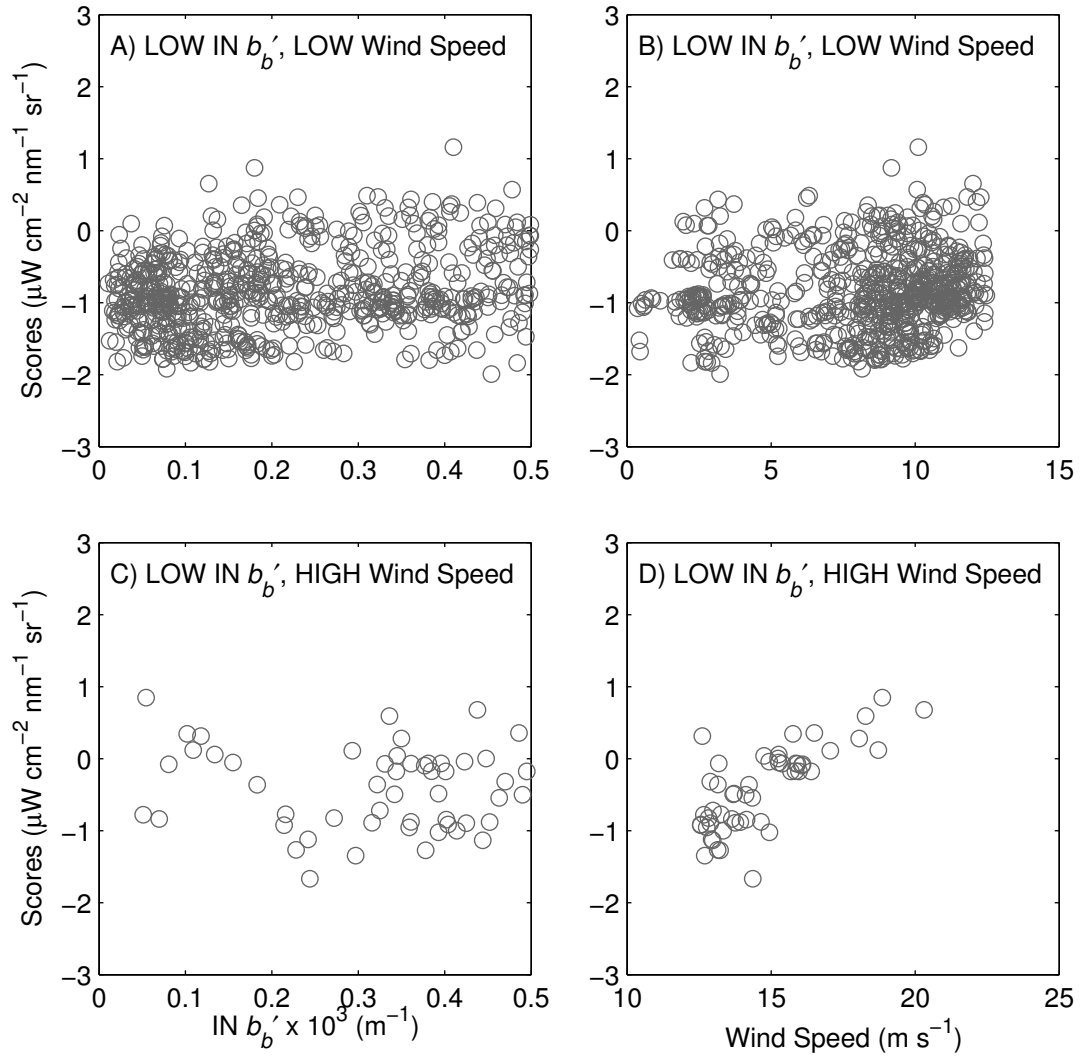
Figure 3.9. A and C) scores of the first OUT $nL_w$ EOF versus IN $b_b'$ for the two LOW IN $b_b'$ scenarios. B and D) scores of the first OUT $nL_w$ EOF versus wind speed for the two LOW IN $b_b'$ scenarios. Refer to Tables 3.2 and 3.3 for the corresponding Pearson correlation coefficients.
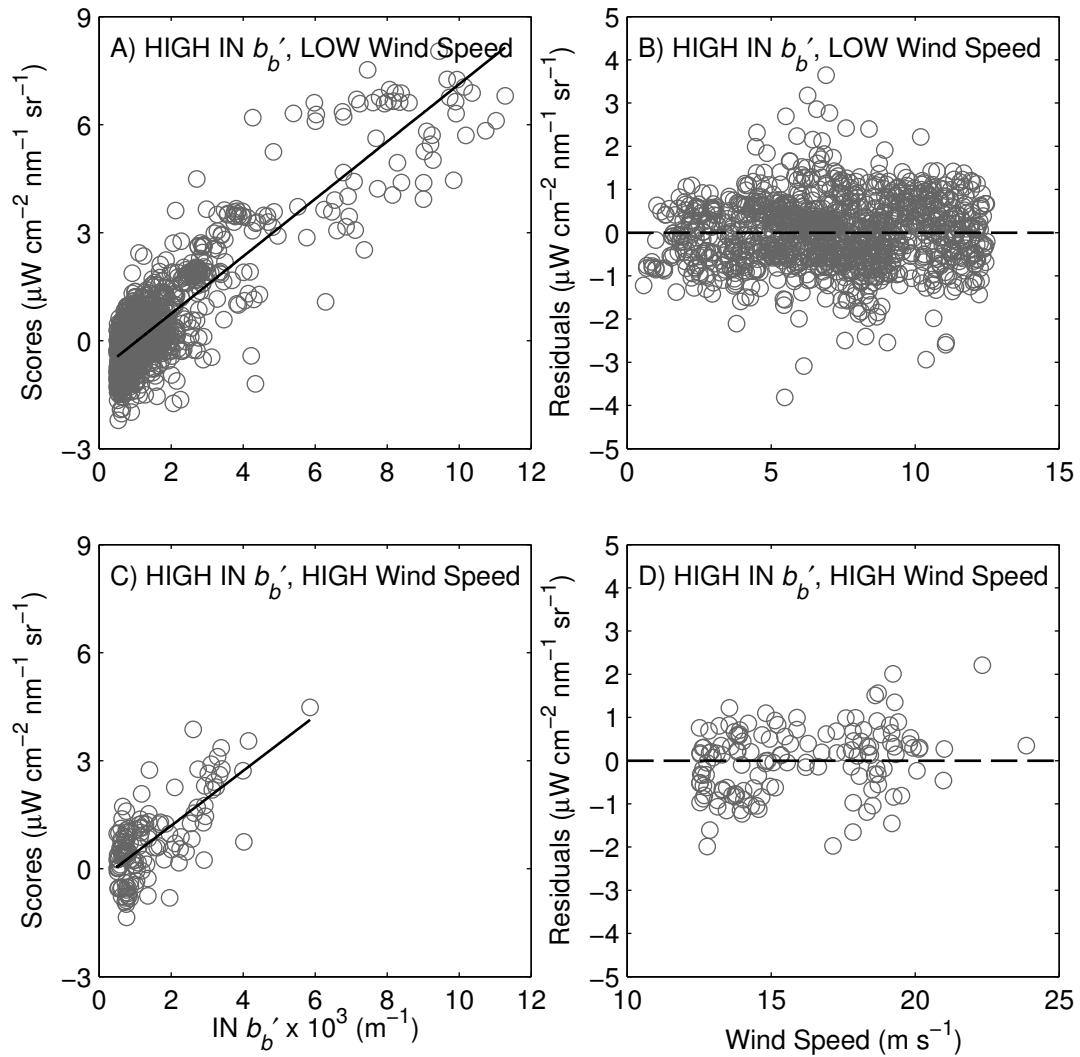
Figure 3.10. A and C) scores of the first OUT $nL_w$ EOF versus IN $b_b'$ for the two HIGH IN $b_b'$ scenarios. The solid black lines are the least-squares regression lines. B and D) residuals of the linear regressions in A and C, respectively, versus wind speed for the two HIGH IN $b_b'$ scenarios. The dashed black lines are the zero reference lines. Refer to Tables 3.2 and 3.3 for the corresponding Pearson correlation coefficients.

**3.8 Wind Speed Elevation of Above-Water PIC Backscattering**

As with the scores, a positive correlation between OUT $b_b'$ and wind speed would have suggested an elevation of OUT $b_b'$ due to wind speed, and therefore entrained bubbles. However, there was no apparent relationship between these variables (Figure 3.11A). For a given wind speed, increasing values of OUT $b_b'$ were generally associated with increasing values of IN $b_b'$, as indicated by the horizontal bands of color. Indeed, a clear positive correlation was apparent between OUT $b_b'$ and IN $b_b'$, although this relationship existed primarily at IN $b_b'$ approximately $> 5 \times 10^{-4}$ m$^{-1}$ (Figure 3.11B). For a given IN $b_b'$ value, increasing values of OUT $b_b'$ were not associated with increasing wind speed, as indicated by the absence of horizontal bands of color.

To further investigate the relationship between OUT $b_b'$ and wind speed, the dataset was again isolated into four combinations of low and high IN $b_b'$ and wind speed. The previous threshold values of $5 \times 10^{-4}$ m$^{-1}$ and 12.5 m s$^{-1}$ were used for IN $b_b'$ and wind speed, respectively. As with the scores, for each of these four scenarios the Pearson correlation coefficient was computed between OUT $b_b'$ and IN $b_b'$ ($r_{OUT,IN}$; dimensionless). Statistical significance was again defined at $\alpha = 0.05$ based on $p_{adj}$ (Appendix A), and OUT $b_b'$ and IN $b_b'$ were log-transformed to yield a linear relationship. If $r_{OUT,IN}$ was significant, a least-squares linear regression model was constructed using IN $b_b'$ and OUT $b_b'$ as predictor and response variables, respectively. The residuals of this model represented the unexplained variability in OUT $b_b'$. The correlation coefficient was then computed between the residuals and wind speed ($r_{r,w}$; dimensionless) to examine a potential effect of wind speed on OUT $b_b'$. However, if $r_{OUT,IN}$ was not significant, the correlation coefficient was computed between OUT $b_b'$ and wind speed ($r_{OUT,w}$; dimensionless) to examine a potential effect of wind speed on OUT $b_b'$. A positive value of either $r_{r,w}$ or $r_{OUT,w}$ would have suggested an elevation of OUT $b_b'$ due to wind speed (and therefore entrained bubbles).

The results of this analysis are shown in Figures 3.12 and 3.13, and the corresponding statistics are summarized in Tables 3.4 and 3.5. Two primary observations were apparent: 1) the correlation between OUT $b_b'$ and IN $b_b'$ was only significant in the

two HIGH IN $b_b'$ scenarios (LOW wind speed: $r_{OUT,IN}$ = 0.616, HIGH wind speed: $r_{OUT,IN}$ = 0.643; Table 3.4, Figures 3.12A and C and 3.13A and C) and 2) neither the correlation between the residuals and wind speed or the correlation between OUT $b_b'$ and wind speed were significant in any of the four scenarios (Table 3.5, Figures 3.12B and D and 3.13B and D). Therefore, OUT $b_b'$ was only correlated with IN $b_b'$ at values of IN $b_b' > 5x10^{-4}$ $m^{-1}$, and there was no elevation of OUT $b_b'$ due to wind speed in any combination of wind speed and IN $b_b'$.

Table 3.4. Pearson correlation coefficients between OUT $b_b'$ and IN $b_b'$ ($r_{OUT,IN}$) for the four scenarios of LOW and HIGH IN $b_b'$ and wind speed. Here $n_{eff}$ and $p_{adj}$ are the sample size ($n$; dimensionless) and $p$-value ($p$; dimensionless), respectively, adjusted for any autocorrelation present in the data (Appendix A). Bolded correlations are significant at $\alpha$ = 0.05 based on $p_{adj}$.

| IN $b_b'$ | Wind Speed | $r_{OUT,IN}$ | $n$ | $p$ | $n_{eff}$ | $p_{adj}$ |
|---|---|---|---|---|---|---|
| LOW | LOW | 0.051 | 535 | 0.240 | 22 | 0.820 |
| LOW | HIGH | -0.387 | 51 | 0.005 | 14 | 0.146 |
| HIGH | LOW | **0.616** | **1173** | **< 0.001** | **38** | **< 0.001** |
| HIGH | HIGH | **0.643** | **138** | **< 0.001** | **14** | **0.015** |

Table 3.5. Pearson correlation coefficients between the residuals and wind speed ($r_{r,w}$) or OUT $b_b'$ and wind speed ($r_{OUT,w}$) for the four scenarios of LOW and HIGH IN $b_b'$ and wind speed. Here $n_{eff}$ and $p_{adj}$ are the sample size ($n$; dimensionless) and $p$-value ($p$; dimensionless), respectively, adjusted for any autocorrelation present in the data (Appendix A). Bolded correlations are significant at $\alpha$ = 0.05 based on $p_{adj}$.

| IN $b_b'$ | Wind Speed | $r_{r,w}$ | $r_{OUT,w}$ | $n$ | $p$ | $n_{eff}$ | $p_{adj}$ |
|---|---|---|---|---|---|---|---|
| LOW | LOW | - | 0.287 | 535 | < 0.001 | 15 | 0.265 |
| LOW | HIGH | - | 0.257 | 51 | 0.069 | 9 | 0.448 |
| HIGH | LOW | 0.177 | - | 1173 | < 0.001 | 31 | 0.333 |
| HIGH | HIGH | 0.182 | - | 138 | 0.033 | 8 | 0.601 |
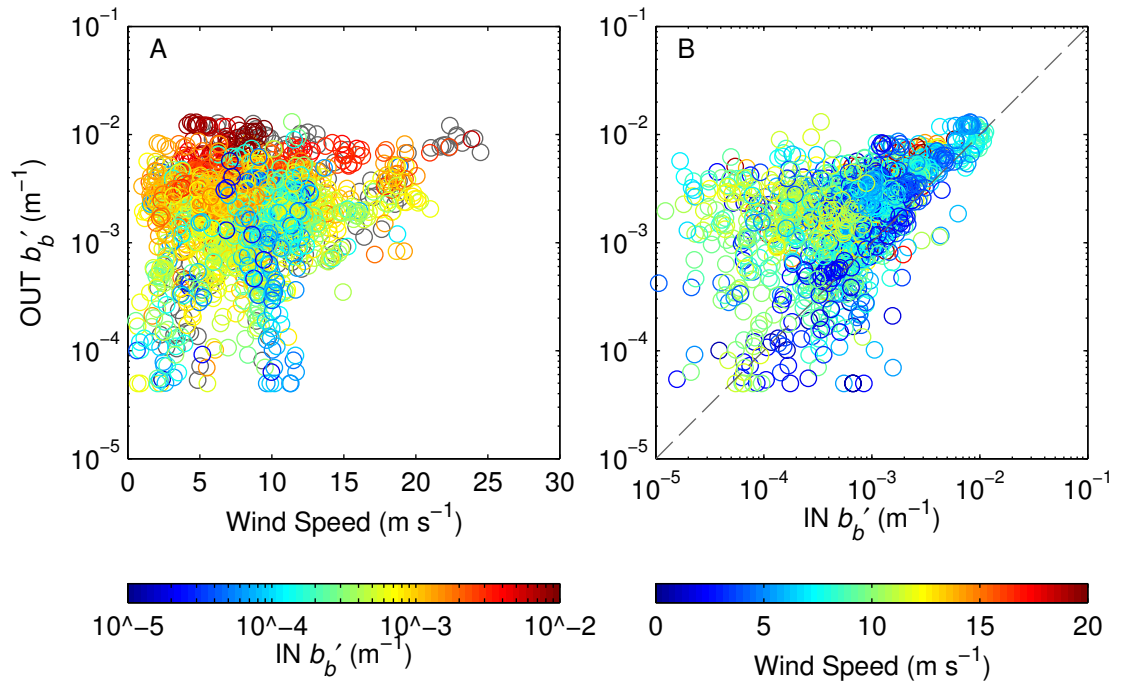
Figure 3.11. OUT $b_b'$ versus A) wind speed and B) IN $b_b'$. The dashed gray line is the 1:1 line. Data points in panels A and B are colored according to the coincident IN $b_b'$ values and wind speeds, respectively, where gray indicates missing values.
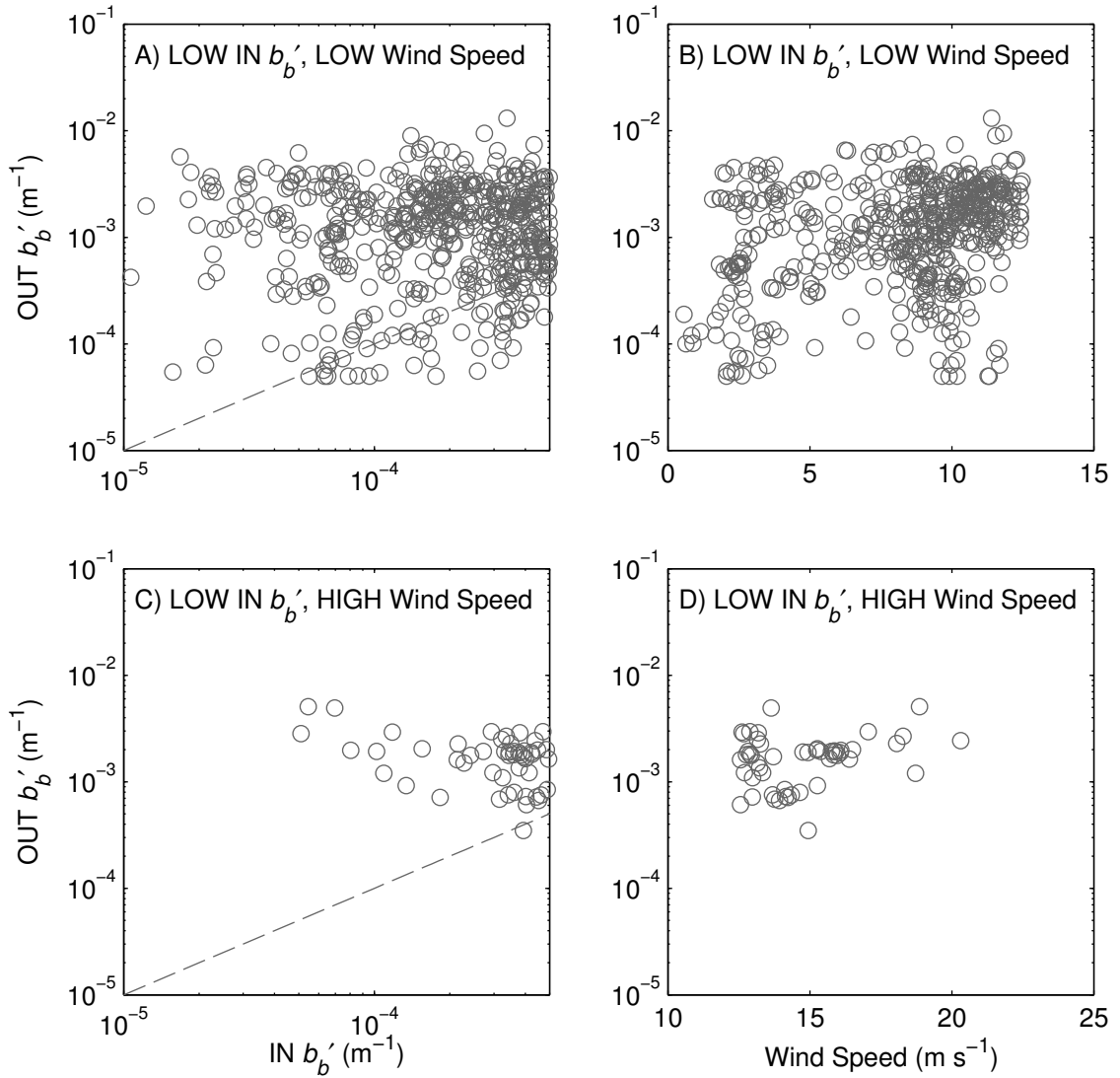
Figure 3.12. A and C) OUT $b_b'$ versus IN $b_b'$ for the two LOW IN $b_b'$ scenarios. The dashed gray lines are the 1:1 lines. B and D) OUT $b_b'$ versus wind speed for the two LOW IN $b_b'$ scenarios. Refer to Tables 3.4 and 3.5 for the corresponding Pearson correlation coefficients.
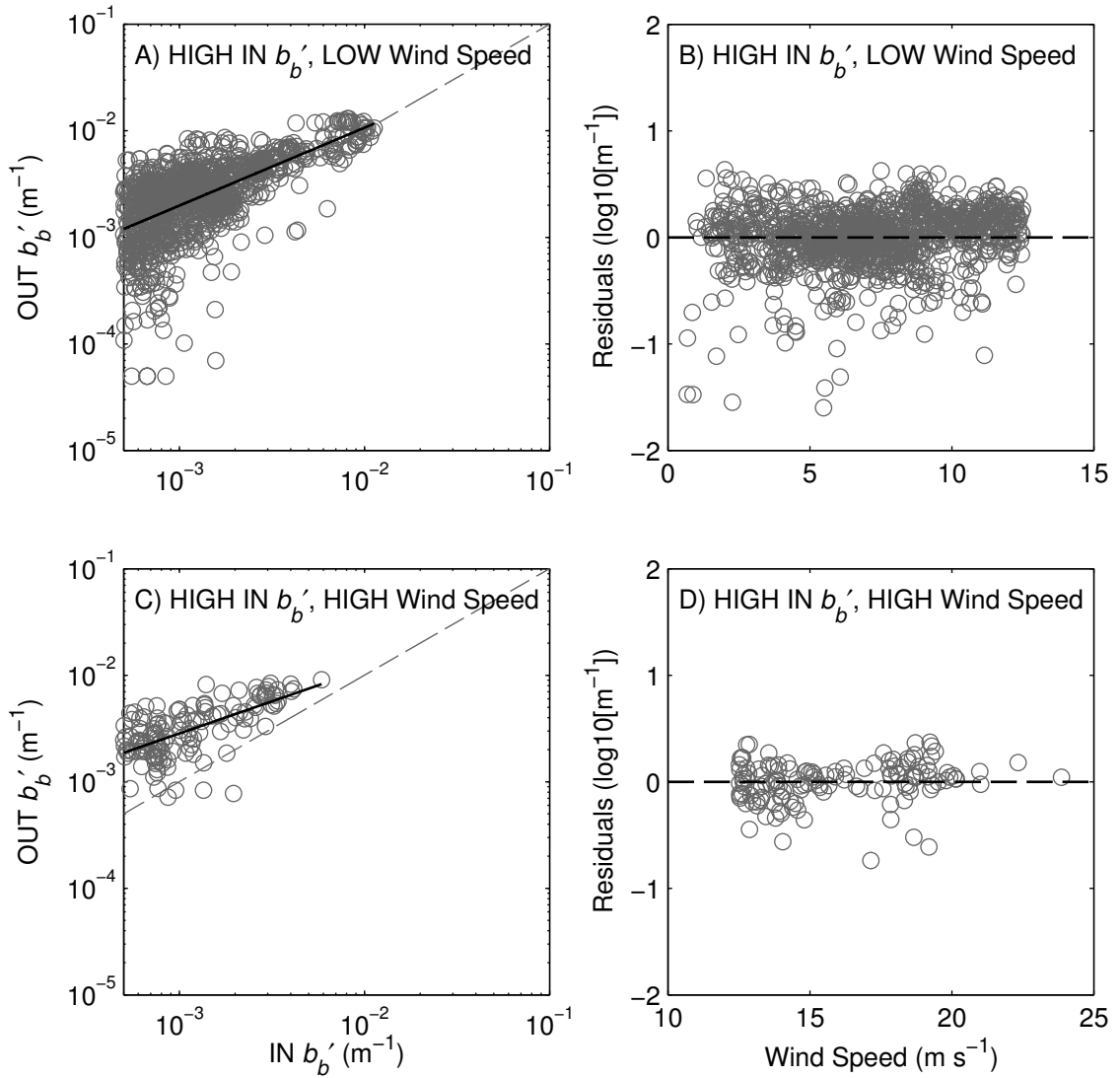
Figure 3.13. A and C) OUT $b_b'$ versus IN $b_b'$ for the two HIGH IN $b_b'$ scenarios. The solid black lines are the least-squares regression lines. The dashed gray lines are the 1:1 lines. B and D) residuals of the linear regressions in A and C, respectively, versus wind speed for the two HIGH IN $b_b'$ scenarios. The dashed black lines are the zero reference lines. Refer to Tables 3.4 and 3.5 for the corresponding Pearson correlation coefficients.

CHAPTER 4

DISCUSSION

**4.1 Above-Water Radiometry Accuracy**

There was confidence in the accuracy of the OUT $nL_w$ spectra. The SAT $nL_w$ spectra were used for an independent verification. The results of comparing their magnitude at common wavelengths (Table 3.1) were similar to those reported by Bailey and Werdell (2006) for a global dataset of $nL_w$. In that study the MR was consistently within 10% of unity, with a typical SIQR of about 0.15, and a negative bias in the satellite data was also evident. Furthermore, the MPD ranged from 13.74 to 24.09%, there was a systematic decrease in the regression slopes with wavelength, the furthest deviation of the slope from unity was 1.146, the $r^2$ was consistently above 0.800, and the typical RMSE was ~0.225 $\mu$W cm$^{-2}$ nm$^{-1}$ sr$^{-1}$. Additionally, the dominant shape of the OUT $nL_w$ and SAT $nL_w$ spectra were similar, characterized by a maximum around 490 nm in the blue region of the spectrum, followed by a minimum at longer wavelengths (Figures 3.4A and 3.6A). When normalized by their integral, both datasets showed a secondary shape, which was characterized by a maximum around 555 nm in the green region of the spectrum and associated with lower values of IN $b_b'$ (Figures 3.4B and 3.6B). Both of these shapes were evident in the hyperspectral $R_{rs}$ spectra reported by Garcia et al. (2011), who observed a PS coccolithophore bloom further to the west in January 2008.

**4.2 PIC as a Dominant Optically Active Seawater Constituent**

The PS coccolithophore bloom peaked north of the FIs between 24 November and 1 December, and was substantially reduced in size and intensity when it was initially observed about three weeks later on 19 December during the COPAS'08 cruise (Painter et al. 2010). The portion of the bloom encircling the FIs to the east and south formed

later, peaking between 18 and 25 December. Overall this feature represented the maximum coccolithophore concentration in the region for eight months (Balch et al. accepted). Bloom waters were dominated by the *E. huxleyi* morphotype B/C (Poulton et al. 2011). Other notable features that were observed in the IN $b_b'$ dataset included a subordinate bloom located to the northwest of the FIs, likely due to a band of stratified water trapped between two tidal fronts (Balch et al. accepted). This bloom was probably similar to the feature observed by Garcia et al. (2011). Additionally, the elevated values of IN $b_b'$ observed as far north of the FIs as 42.5°N were a result of water rich in PIC being carried northwards by the Falklands Current. Throughout the cruise IN $b_b'$ showed similar spatial patterns to PIC concentration determined by Inductively-Coupled Plasma Optical Emission Spectroscopy (Balch et al. accepted). This provided confidence that IN $b_b'$ was an appropriate indicator of PIC.

Multiple lines of evidence were presented in this study demonstrating that PIC was a dominant optically active seawater constituent at higher concentrations. The first OUT $nL_w$ EOF represented the primary mode of spectral variability, accounting for 95% of the dataset variance, and was due to changes in spectral amplitude (Figure 3.5). Elevated spectra were clearly associated with higher values of IN $b_b'$ (Figure 3.4A). Furthermore, the scores of the first EOF, which could be physically interpreted as indices of spectral amplitude, were positively correlated with IN $b_b'$ in the two HIGH IN $b_b'$ scenarios (LOW wind speed: $r_{s,IN} = 0.867$; HIGH wind speed: $r_{s,IN} = 0.705$; Table 3.2, Figure 3.10A and C). Assuming $b_b* = 4$ m$^2$ mol$^{-1}$, the threshold IN $b_b'$ value of $5 \times 10^{-4}$ m$^{-1}$ is equivalent to ~2 µgPIC L$^{-1}$ (Equation 1.3), which is the global average PIC concentration (Balch et al. 2005). Above this threshold PIC was clearly a dominant driver of OUT $nL_w$ spectral variability. These results are consistent with those of Garcia et al. (2011), who performed an EOF analysis on their $R_{rs}$ spectra. In that study the first EOF resembled the dominant spectral shape and accounted for 98% of the dataset variance. Furthermore, the authors found a positive correlation (0.77) between the scores of the first EOF and PIC concentrations ranging from ~35 to 300 µgPIC L$^{-1}$. Given the strong backscattering properties of coccoliths, it is not surprising that PIC was a dominant optically active constituent at higher concentrations during the cruise.

However, the scores were not correlated with IN $b_b'$ in the two LOW IN $b_b'$ scenarios (Table 3.2, Figure 3.9A and C). This indicates that below the threshold of ~2 µgPIC L$^{-1}$ PIC did not drive OUT $nL_w$ spectral variability, suggesting that it might have been difficult to detect optically. Indeed, although OUT $b_b'$ was positively correlated with IN $b_b'$ in the two HIGH IN $b_b'$ scenarios (LOW wind speed: $r_{OUT,IN}$ = 0.616; HIGH wind speed: $r_{OUT,IN}$ = 0.643; Table 3.4, Figure 3.13A and C), it was not correlated with IN $b_b'$ in the two LOW IN $b_b'$ scenarios (Table 3.4, Figure 3.12A and C). As was observed, OUT $b_b'$ was generally elevated compared to IN $b_b'$ (Figures 3.1A and C, 3.2A, 3.3A and C, and 3.11B). However, the RMSE of the two-band PIC algorithm in this application was ~2x10$^{-3}$ m$^{-1}$, equivalent to ~6 µgPIC L$^{-1}$ assuming $b_b^*$ = 4 m$^2$ mol$^{-1}$, which is well within the published RMSE of 28 µgPIC L$^{-1}$ (Balch et al. 2005). Interestingly, the fact that the scores were correlated with higher values of IN $b_b'$ suggests that an alternative PIC algorithm could be constructed with the EOF methodology of Craig et al. (2012). This is something that I will actively pursue in the future.

## 4.3 Limited Impact of Bubbles

There was limited evidence to suggest that wind-generated entrained bubble populations elevated OUT $nL_w$ during the cruise. In the two LOW IN $b_b'$ scenarios the scores of the first OUT $nL_w$ EOF were only correlated with wind speed in the HIGH wind speed scenario ($r_{s,w}$ = 0.755; Table 3.3, Figure 3.9B and D). Indeed, it was expected that this would be the most likely scenario for bubbles to elevate OUT $nL_w$, given the higher wind speeds and minimal elevation of the spectra due to PIC. However, this result should be interpreted cautiously. The correlation was sensitive to the wind speed threshold used. For example, it was no longer significant if the threshold was reduced from 12.5 to 12.0 m s$^{-1}$. Additionally, in the two HIGH IN $b_b'$ scenarios there was no evidence that bubbles elevated OUT $nL_w$, even in the HIGH wind speed scenario, as there was no correlation between the residual variability of the scores and wind speed (Table 3.3, Figure 3.10B and D). In contrast to OUT $nL_w$, there was no evidence that bubbles elevated OUT $b_b'$ in any of the four scenarios. Specifically, OUT $b_b'$ was not correlated with wind speed in

either of two LOW IN $b_b'$ scenarios (Table 3.5, Figure 3.12B and D). Furthermore, there was no correlation between the residual variability of OUT $b_b'$ and wind speed in either of the two HIGH IN $b_b'$ scenarios (Table 3.5, Figure 3.13B and D). This may suggest that the elevation of OUT $nL_w$ observed in the LOW IN $b_b'$, HIGH wind speed scenario was obscured by errors inherent to the two-band PIC algorithm.

Since no measurements of bubbles were made in this study, it is not possible to definitively confirm their presence or absence during the cruise. One ramification of this is that it is not possible to directly link the correlation between the scores and wind speed in the LOW IN $b_b'$, HIGH wind speed scenario to bubbles, rather than a different phenomenon mediated by wind speed (whitecaps, ship roll, etc.). However, it is likely that bubbles were present throughout the cruise, even in the LOW wind speed scenarios (wind speed < 12.5 m s$^{-1}$). For example, during wind speeds > 3 m s$^{-1}$ bubble entrainment is the dominant source of bubbles in the surface ocean in the absence of precipitation (Thorpe 1992). Additionally, during wind speeds > 7 m s$^{-1}$ separate bubble plumes near the sea surface join and produce a stratus layer (Thorpe 1995). Furthermore, Randolph et al. (2014) observed wind-generated entrained bubble populations during wind speeds of ~13 m s$^{-1}$ as part of the SO GasEx expedition.

Given the impact of bubbles on surface ocean optics demonstrated in the literature (e.g. Stramski 1994, Zhang et al. 1998, Stramski and Tegowski 2001), it is surprising that in my study there was only limited evidence for an elevation of OUT $nL_w$ due to bubbles, even in the HIGH wind speed scenarios (wind speed > 12.5 m s$^{-1}$). One possible explanation for this is that most of the impact of bubbles was removed during the above-water radiometry quality control procedure. As described above, only the lowest 5% of the above-water radiometry in each temporal bin (~6 minutes) was accepted. This is a routine procedure, and is performed to eliminate the effects of whitecaps and sun glint (Mueller et al. 2003). It has been demonstrated that the optical impacts of bubbles can be highly variable over time periods of minutes or less (Stramski and Tegowski 2001, Terrill et al. 2001), and therefore it is possible that they could be removed during this procedure. There have been few field studies that have verified an elevation of $nL_w$ or $R_{rs}$ due to entrained bubbles. Zhang et al. (2004) observed elevated in-water and airborne $R_{rs}$ due to bubbles entrained by ship wakes in the equatorial Pacific and offshore of New Jersey.

Additionally, Randolph et al. (2010) observed elevated in-water and above-water $R_{rs}$ due to wind-generated entrained bubbles in the Atlantic Sector of the Southern Ocean during wind speeds of 13 to 15 m s$^{-1}$. However, in-water measurements of $R_{rs}$ do not require the removal of whitecaps or sun glint, and the airborne and above-water measurements of $R_{rs}$ by Zhang et al. (2004) and Randolph et al. (2010), respectively, did not employ quality control procedures to remove whitecaps or sun glint.

The results of my study suggest that wind-generated entrained bubble populations can possibly elevate measurements of quality-controlled above-water $nL_w$ at wind speeds > 12.5 m s$^{-1}$. However, there is no evidence that bubbles elevate estimates of PIC made using the two-band PIC algorithm (Balch et al. 2005) at the wind speeds observed during the cruise (0 to 25 m s$^{-1}$). Future work should verify if routine quality control procedures applied to above-water radiometry measurements, which are designed to remove whitecaps and sun glint, also remove entrained bubbles. This could be done with concurrent field measurements of bubbles and above-water $nL_w$ or $R_{rs}$, in combination with radiative transfer modeling. These results also have implications for satellite radiometry measurements, e.g. those in the GCB, as an attempt is made to remove whitecaps in standard satellite atmospheric correction procedures (Gordon and Wang 1994b). These procedures could also remove entrained bubbles, which should be verified in future work. Overall, the results of my study emphasize the need to consider the practical use of $nL_w$ or $R_{rs}$ when assessing the optical impacts of bubbles. If bubbles are removed from above-water or satellite measurements during routine quality control or atmospheric correction procedures, their impacts could be minimal.

CHAPTER 5


**CONCLUSION**


In December 2008 the COPAS'08 cruise observed a mesoscale coccolithophore bloom on the PS, the brightest region of the GCB. Observations made during the cruise provided an opportunity to determine if wind-generated entrained bubble populations elevated measurements of above-water $nL_w$ and subsequent remote sensing estimates of PIC. The first OUT $nL_w$ EOF accounted for 95% of the dataset variance, and was attributed to changes in spectral amplitude. Scores of the first EOF were positively correlated with IN $b_b' > 5 \times 10^{-4}$ m$^{-1}$, regardless of wind speed. This indicated that PIC was an optically active seawater constituent above this threshold. However, there was limited evidence to suggest that bubbles elevated OUT $nL_w$, and no evidence that they elevated OUT $b_b'$. This is in contrast to the results of previous studies that have demonstrated the impact of bubbles on surface ocean optics (e.g. Stramski 1994, Zhang et al. 1998, Stramski and Tegowski 2001). The results of this study are primarily applicable to above-water $nL_w$ or $R_{rs}$ measurements (i.e. not in-water or satellite) employing routine quality control procedures to remove sun glint and whitecaps. Future studies should expand upon this by incorporating field measurements of bubble concentration, in combination with radiative transfer modeling, to compare observed and modeled $nL_w$ or $R_{rs}$. This should provide insight into, among other things, whether quality controls for sun glint and whitecaps are simultaneously removing the impact of bubbles.

APPENDIX A

## NOTE ON AUTOCORRELATION

The time series of both IN $b_b'$ and wind speed were autocorrelated, as indicated by their respective autocorrelation functions (Figure A.1). It was not possible to directly diagnose the presence of autocorrelation in the time series of the scores of the first OUT $nL_w$ EOF and OUT $b_b'$ due to the nighttime gaps in the data. Instead, it was assumed that they had an autocorrelation structure similar to that of IN $b_b'$. Autocorrelation indicates that future values of a variable are dependent on its previous values. Indeed, because they were measured continuously during the cruise, it was expected that these variables would be autocorrelated. However, classical statistical tests assume independent data. Application of these tests without considering the effects of autocorrelation can result in incorrect conclusions.

I took great care to develop a parsimonious analysis that was both effective and accounted for the autocorrelated data. The analysis consisted of first isolating the complete time series of the variables into four scenarios of low and high IN $b_b'$ and wind speed. For each scenario the Pearson correlation coefficient was then computed between various pairs of variables. To appreciate the effect of autocorrelation on these correlation coefficients, consider the vectors $X$ and $Y$ (dimensionless), each of sample size $n_{X,Y}$ (dimensionless). These vectors are analogous to the complete time series of the variables. Additionally, consider the vectors $x$ and $y$ (dimensionless), *aligned* segments of $X$ and $Y$, each of sample size $n_{x,y}$ (dimensionless) $<< n_{X,Y}$. These vectors are analogous to the variables once they were isolated into the four scenarios of low and high IN $b_b'$ and wind speed. The sample correlation of $x$ and $y$ ($r_{x,y}$; dimensionless) has approximately a normal distribution with a standard deviation ($\sigma_{x,y}$; dimensionless) given according to:

$$\sigma_{x,y} = \frac{1-\rho_{x,y}^2}{\sqrt{n_{x,y}}} \tag{A.1}$$

where $\rho_{x,y}$ (dimensionless) is the true correlation of $x$ and $y$. Under the null hypothesis that $\rho_{x,y}$ is zero, the distribution of $r_{x,y}$ has a mean of zero, and Equation A.1 simplifies according to:

$$\sigma_{x,y} = \frac{1}{\sqrt{n_{x,y}}} \tag{A.2}$$

If either $x$ or $y$ is autocorrelated, then the effective standard deviation of $r_{x,y}$ ($\sigma_{x,y,eff}$; dimensionless) is approximated according to:

$$\sigma_{x,y,eff} = \frac{1}{\sqrt{n_{x,y,eff}}} \tag{A.3}$$

where $n_{x,y,eff}$ (dimensionless) is the effective sample size of $x$ and $y$, and $n_{x,y,eff} < n_{x,y}$ since the data are not independent. Taking the ratio of $\sigma_{x,y,eff}$ to $\sigma_{x,y}$ indicates that the autocorrelation present in either $x$ or $y$ effectively increases $\sigma_{x,y}$. The larger standard deviation makes the tail of the sampling distribution of $r_{x,y}$ under the null hypothesis heavier than would be expected for independent data. Therefore, by not taking autocorrelation into account, test $p$-values will be underestimated. The effect of this increase in $\sigma_{x,y}$ can be quantified if the autocorrelation structures of $x$ and $y$ are relatively simple, for example if the variables can be modeled as first-order autoregressive (AR(1)) processes. In the present study wind speed could be modeled as an AR(1) process (Figure A.1A). This is often the case for daily meteorological variables (Wilks 2006). However, IN $b_b{}'$ could not be modeled as an AR(1) process (Figure A.1B), and therefore it was assumed that the scores and OUT $b_b{}'$ could not either.

Given that the autocorrelation structures of IN $b_b{}'$, the scores, and OUT $b_b{}'$ were unknown, a novel resampling method was developed to assess the statistical significance of $r_{x,y}$. To estimate the sampling distribution of $r_{x,y}$ under the null hypothesis, $1\times10^5$ pairs of *unaligned* segments ($x'$ and $y'$; dimensionless) were randomly resampled (with replacement) from $X$ and $Y$. For each pair of $x'$ and $y'$ the correlation coefficient ($r_{x,y}{}'$; dimensionless) was computed. The resulting $1\times10^5$ values of $r_{x,y}{}'$ provided an empirical distribution that was used to estimate $n_{x,y,eff}$ and an adjusted $p$-value ($p_{adj}$; dimensionless) for $r_{x,y}$ under the null hypothesis.

51

The resampling method was applied to four test cases of simulated data, where $X$ and $Y$ were: 1) independent processes and not correlated, 2) independent processes and correlated, 3) AR(1) processes and not correlated, and 4) AR(1) processes and correlated. To be consistent with the present study, $X$ and $Y$ were chosen to be of length $n_{X,Y} = 5000$, the approximate sample size of IN $b_b{'}$ and wind speed. Additionally, $x$ and $y$ were chosen to be of length $n_{x,y} = 500$, the average sample size of the low and high IN $b_b{'}$ and wind speed scenarios (Tables 3.2, 3.3, 3.4, and 3.5). For each test case of simulated data the resampling method yielded the expected results. In the first test case $n_{x,y,eff}$ was determined to be ~500 and $p_{adj}$ indicated that $r_{x,y}$ was not significant ($X$ and $Y$ were independent processes and not correlated; Table A.1, Figure A.2). In the second test case $n_{x,y,eff}$ was again computed to be ~500, but $p_{adj}$ correctly indicated that $r_{x,y}$ was significant ($X$ and $Y$ were independent processes and correlated; Table A.1, Figure A.3). In the third test case $n_{x,y,eff}$ was computed to be $< 500$ and $p_{adj}$ indicated that $r_{x,y}$ was not significant, therefore preventing a Type I error, i.e. a false positive ($X$ and $Y$ were AR(1) processes and not correlated; Table A.1, Figure A.4). In the fourth test case $n_{x,y,eff}$ was again computed to be $< 500$, but $p_{adj}$ correctly indicated that $r_{x,y}$ was significant ($X$ and $Y$ were AR(1) processes and correlated; Table A.1, Figure A.5).

In practice the autocorrelation structure of IN $b_b{'}$ was used to approximate that of the scores and OUT $b_b{'}$, as well as the residuals of the regressions of the scores onto IN $b_b{'}$ and OUT $b_b{'}$ onto IN $b_b{'}$. Additionally, because $X$ and $Y$ were not subset according to time, but rather IN $b_b{'}$ and wind speed, $x$ and $y$ did not consist of uniformly contiguous data. Therefore, the reported values of $p_{adj}$ (Tables 3.2, 3.3, 3.4, and 3.5) were likely conservative in the sense that the probability of a Type I error was less than the nominal value of 0.05.

Table A.1. Results of the resampling method on the four test cases of simulated data.

| Test Case | $n_{X,Y}$ | $n_{x,y}$[a] | $r_{x,y}$ | $p$ | $n_{x,y,eff}$ | $p_{adj}$ |
|---|---|---|---|---|---|---|
| Independent, Not Correlated | 5000 | 500 | -0.007 | 0.870 | 496 | 0.872 |
| Independent, Correlated | 5000 | 500 | 0.720 | < 0.001 | 496 | < 0.001 |
| AR(1)[b], Not Correlated | 5000 | 500 | -0.145 | 0.001 | 144 | 0.081 |
| AR(1)[b], Correlated | 5000 | 500 | -0.756 | < 0.001 | 104 | < 0.001 |

[a]The first $n_{x,y}$ elements of $X$ and $Y$ were selected for $x$ and $y$.
[b]The AR(1) coefficients of $X$ and $Y$ were 0.85 and 0.65, respectively.
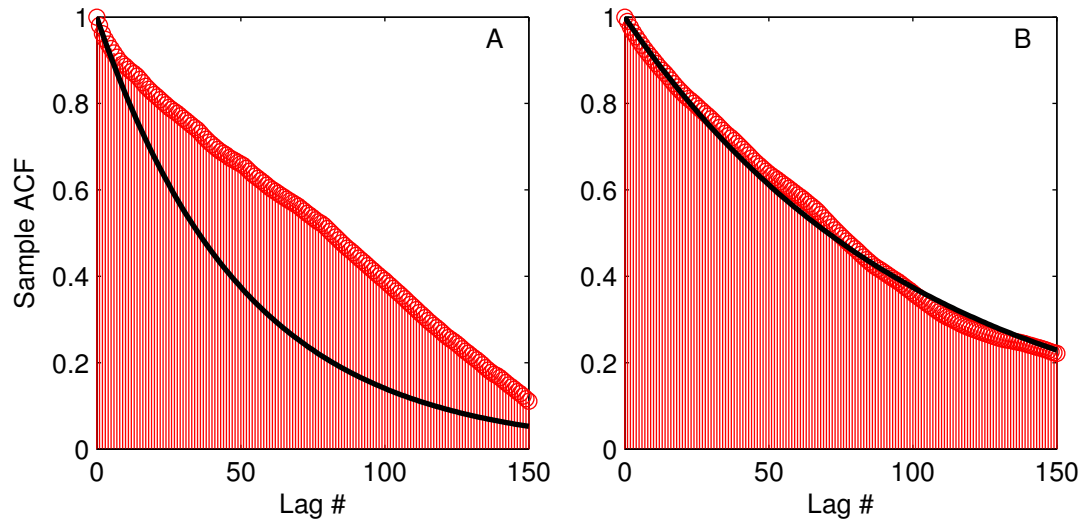
Figure A.1. Autocorrelation function (ACF) of A) IN $b_b{'}$ and B) wind speed. Each lag represents six minutes. The black lines show how the ACFs would appear if an AR(1) process generated the variables.
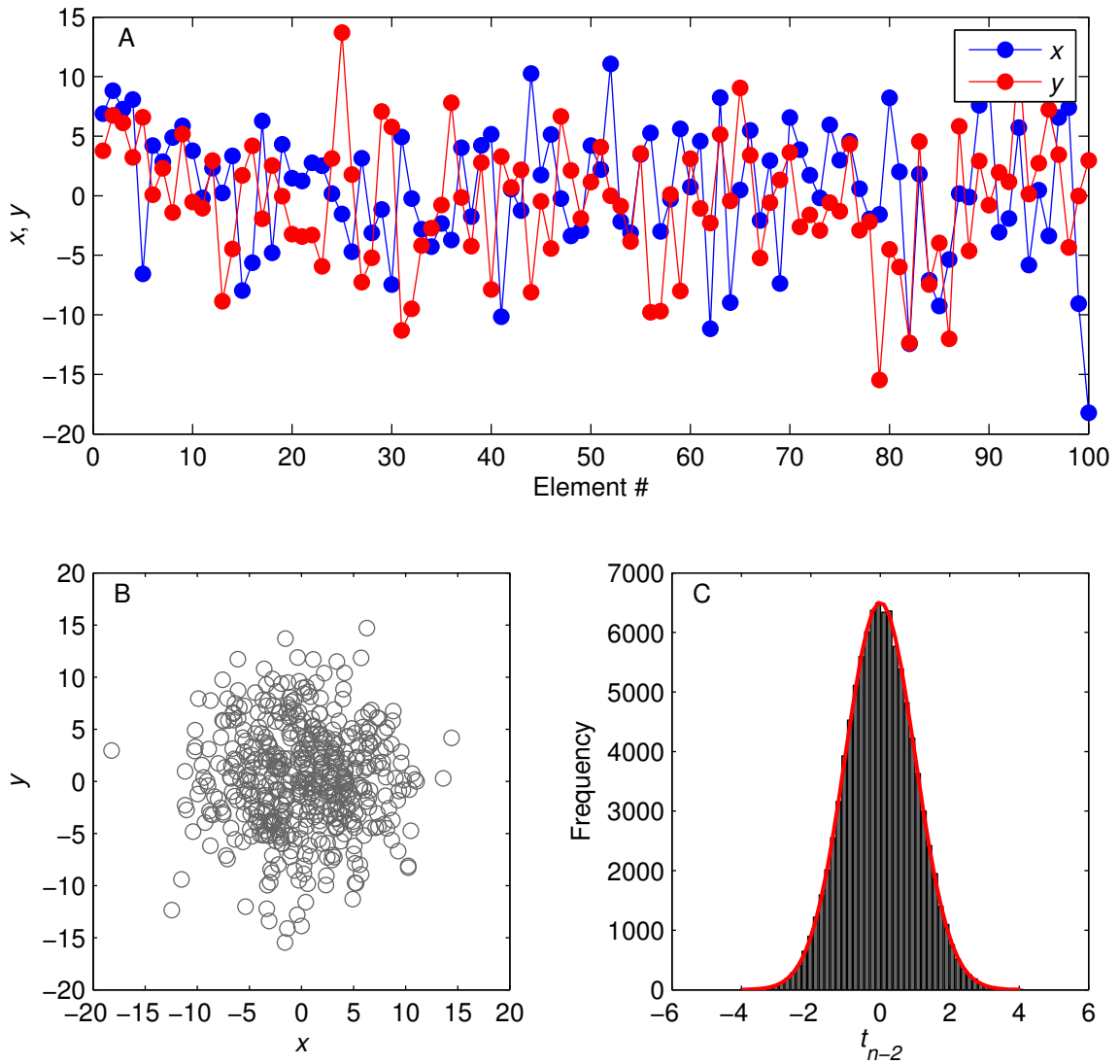
Figure A.2. Results of the resampling method on the first test case of simulated data ($X$ and $Y$ were independent processes and not correlated). A) the first 100 elements of $x$ and $y$, B) $y$ plotted versus $x$, and C) sampling distribution of $r_{x,y}$ under the null hypothesis. The gray bars are the histogram of the $1 \times 10^5$ values of $r_{x,y}'$ computed by the resampling method and converted to Student's t-distribution test statistics. For comparison, the red line is the theoretical t-distribution. The resampled and theoretical distributions agree because $X$ and $Y$ were both independent processes.
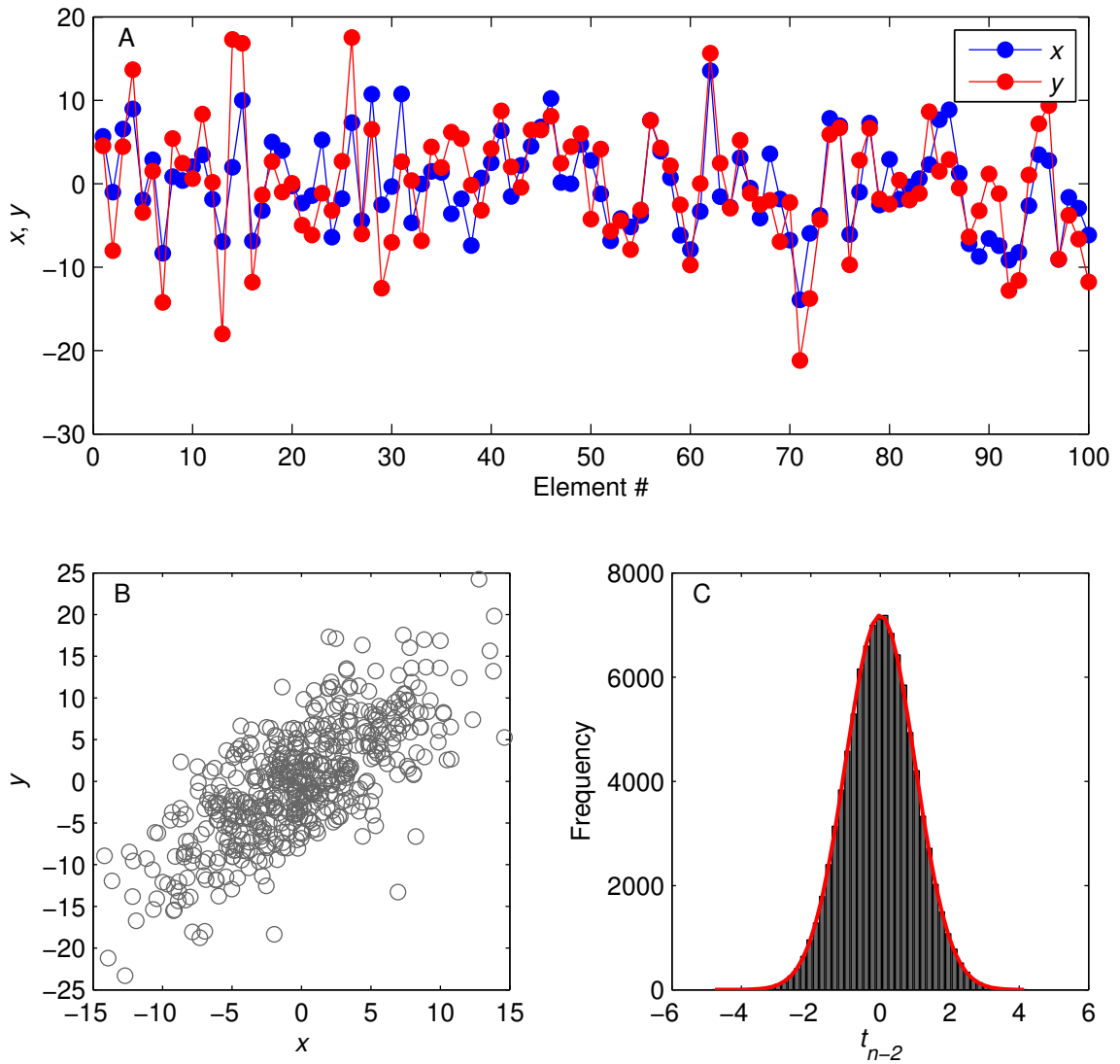
Figure A.3. Results of the resampling method on the second test case of simulated data ($X$ and $Y$ were independent processes and correlated). A) the first 100 elements of $x$ and $y$, B) $y$ plotted versus $x$, and C) sampling distribution of $r_{x,y}$ under the null hypothesis. The gray bars are the histogram of the $1 \times 10^5$ values of $r_{x,y}'$ computed by the resampling method and converted to Student's t-distribution test statistics. For comparison, the red line is the theoretical t-distribution. The resampled and theoretical distributions agree because $X$ and $Y$ were both independent processes.
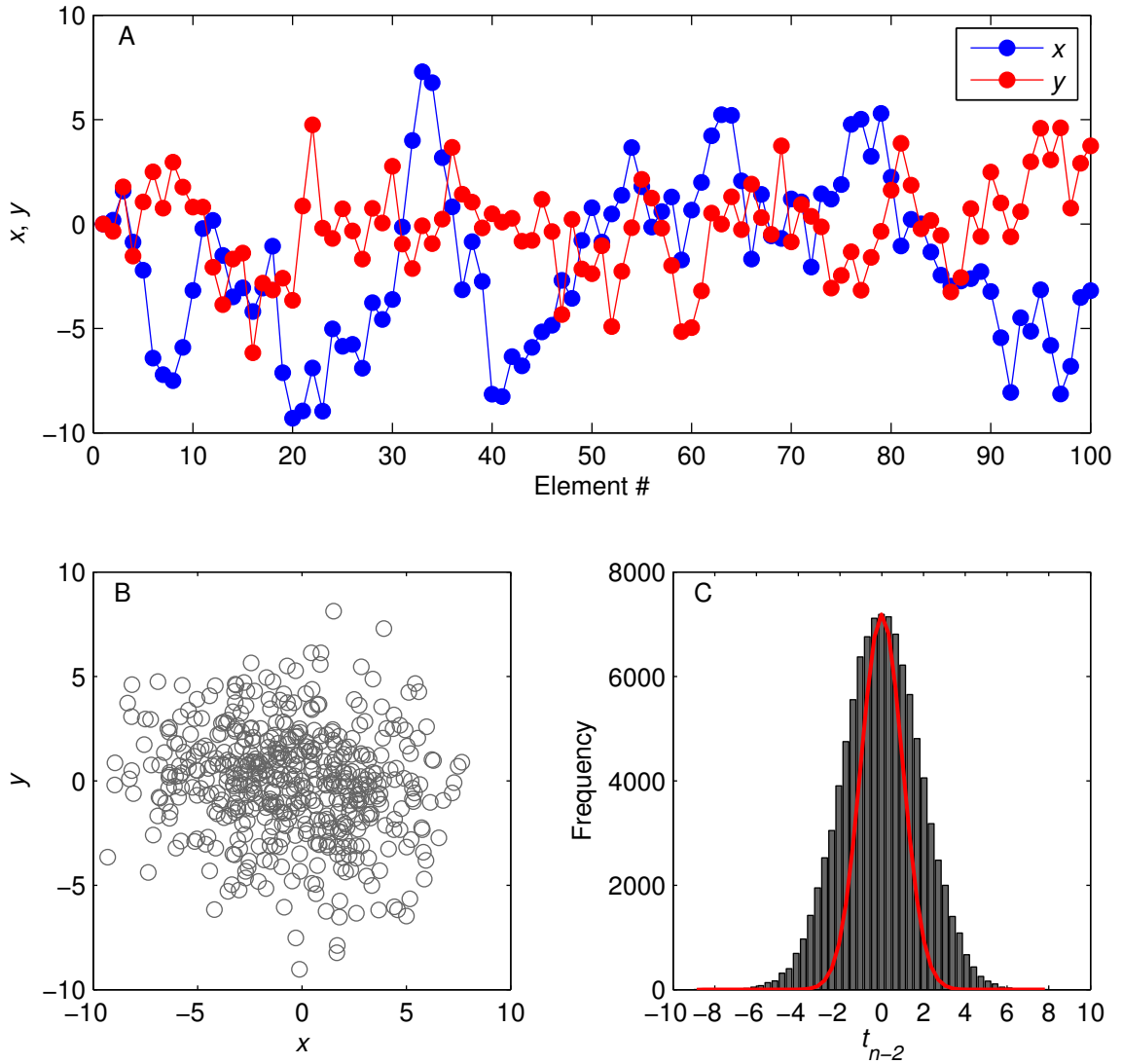
Figure A.4. Results of the resampling method on the third test case of simulated data ($X$ and $Y$ were AR(1) processes and not correlated). A) the first 100 elements of $x$ and $y$, B) $y$ plotted versus $x$, and C) sampling distribution of $r_{x,y}$ under the null hypothesis. The gray bars are the histogram of the $1 \times 10^5$ values of $r_{x,y}'$ computed by the resampling method and converted to Student's t-distribution test statistics. For comparison, the red line is the theoretical t-distribution. The resampled distribution is wider than the theoretical distribution because $X$ and $Y$ were both AR(1) processes.
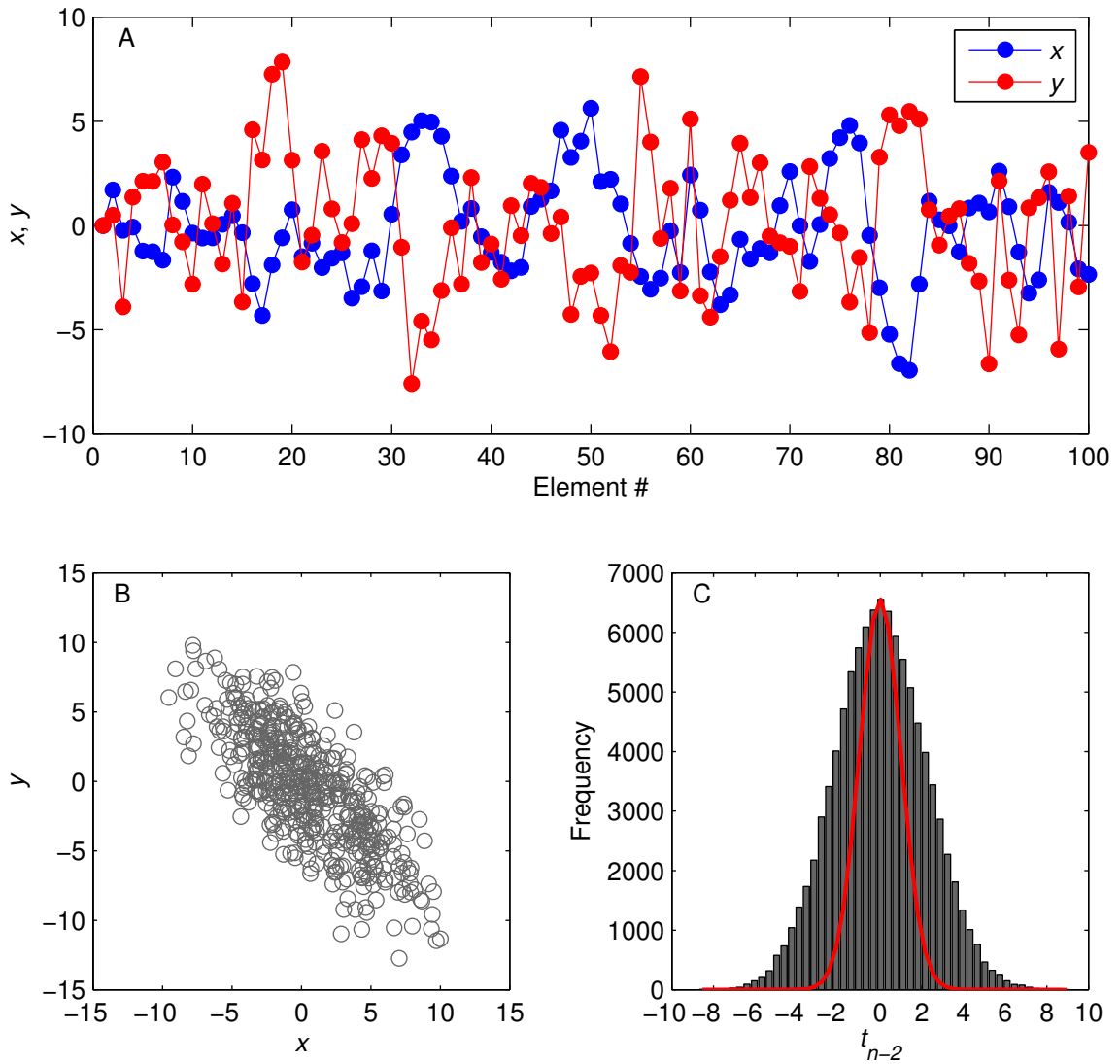
Figure A.5. Results of the resampling method on the fourth test case of simulated data (*X* and *Y* were AR(1) processes and correlated). A) the first 100 elements of *x* and *y*, B) *y* plotted versus *x*, and C) sampling distribution of $r_{x,y}$ under the null hypothesis. The gray bars are the histogram of the $1 \times 10^5$ values of $r_{x,y}'$ computed by the resampling method and converted to Student's t-distribution test statistics. For comparison, the red line is the theoretical t-distribution. The resampled distribution is wider than the theoretical distribution because *X* and *Y* were both AR(1) processes.

58

# BIBLIOGRAPHY

Ackleson S, Balch WM, Holligan PM (1988) White waters of the Gulf of Maine. Oceanography 1:18-22

Ackleson SG, Balch WM, Holligan PM (1994) Response of water-leaving radiance to particulate calcite and chlorophyll-a concentrations: A model for Gulf of Maine coccolithophore blooms. J Geophys Res-Oceans 99:7483-7499

Bailey SW, Werdell PJ (2006) A multi-sensor approach for the on-orbit validation of ocean color satellite data products. Remote Sens Environ 102:12-23

Balch WM, Drapeau DT, Bowler BC, Lyczskowski E, Booth ES, Alley D (2011) The contribution of coccolithophores to the optical and inorganic carbon budgets during the Southern Ocean Gas Exchange Experiment: New evidence in support of the "Great Calcite Belt" hypothesis. J Geophys Res 116:C00F06

Balch WM, Drapeau DT, Cucci TL, Vaillancourt RD, Kilpatrick KA, Fritz JJ (1999) Optical backscattering by calcifying algae: Separating the contribution of particulate inorganic and organic carbon fractions. J Geophys Res-Oceans 104:1541-1558

Balch WM, Gordon HR, Bowler BC, Drapeau DT, Booth ES (2005) Calcium carbonate measurements in the surface global ocean based on Moderate-Resolution Imaging Spectroradiometer data. J Geophys Res 110:C07001

Balch WM, Holligan PM, Ackleson SG, Voss KJ (1991) Biological and optical properties of mesoscale coccolithophore blooms in the Gulf of Maine. Limnol Oceanogr 36:629-643

Balch WM, Kilpatrick KA, Holligan P, Harbour D, Fernandez E (1996a) The 1991 coccolithophore bloom in the central North Atlantic. 2. Relating optics to coccolith concentration. Limnol Oceanogr 41:1684-1696

Balch WM, Kilpatrick KA, Trees CC (1996b) The 1991 coccolithophore bloom in the central North Atlantic. 1. Optical properties and factors affecting their distribution. Limnol Oceanogr 41:1669-1683

Barnes BB, Hu C, Cannizzaro JP, Craig SE, Hallock P, Jones D, Lehrter JC, Melo N, Schaeffer BA, Zepp R (2014) Estimation of diffuse attenuation of ultraviolet light in optically shallow Florida Keys waters from MODIS measurements. Remote Sens Environ 140:519-532

Brown CW, Podestá GP (1997) Remote sensing of coccolithophore blooms in the western south Atlantic Ocean. Remote Sens Environ 60:83-91

Brown CW, Yoder JA (1994) Coccolithophorid blooms in the global ocean. J Geophys Res-Oceans 99:7467-7482

Brownlee C, Taylor A (2004) Calcification in coccolithophores: A cellular perspective. In: Thierstein HR, Young JR (eds) Coccolithophores: From molecular processes to global impact. Springer, Berlin p 31-49

Charlson RJ, Lovelock JE, Andreae MO, Warren SG (1987) Oceanic phytoplankton, atmospheric sulfur, cloud albedo and climate. Nature 326:655-661

Craig SE, Jones CT, Li WKW, Lazin G, Horne E, Caverhill C, Cullen JJ (2012) Deriving optical metrics of coastal phytoplankton biomass from ocean colour. Remote Sens Environ 119:72-83

Falkowski P et al. (2000) The global carbon cycle: A test of our knowledge of earth as a system. Science 290:291-296

Fichot CG, Sathyendranath S, Miller WL (2008) Sea$UV$ and Sea$UV_C$: Algorithms for the retrieval of UV/visible diffuse attenuation coefficients from ocean color. Remote Sens Environ 112:1584-1602

Flatau PJ, Flatau M, Zaneveld JRV, Mobley CD (2000) Remote sensing of bubble clouds in sea water. Q J R Meteorol Soc 126:2511-2523

Frouin R, Schwindling M, Deschamps P-Y (1996) Spectral reflectance of sea foam in the visible and near-infrared: In situ measurements and remote sensing implications. J Geophys Res-Oceans 101:14361-14371

Garcia CAE, Garcia VMT, Dogliotti AI, Ferreira A, Romero SI, Mannino A, Souza MS, Mata MM (2011) Environmental conditions and bio-optical signature of a coccolithophorid bloom in the Patagonian shelf. J Geophys Res 116:C03025

Gordon HR, Boynton GC, Balch WM, Groom SB, Harbour DS, Smyth TJ (2001) Retrieval of coccolithophore calcite concentration from SeaWiFS imagery. Geophys Res Lett 28:1587-1590

Gordon HR, Brown OB, Evans RH, Brown JW, Smith RC, Baker KS, Clark DK (1988) A semianalytic radiance model of ocean color. J Geophys Res-Atmos 93:10909-10924

Gordon HR, Clark DK (1981) Clear water radiances for atmospheric correction of coastal zone color scanner imagery. Appl Opt 20:4175-4180

Gordon HR, Wang M (1994a) Retrieval of water-leaving radiance and aerosol optical thickness over the oceans with SeaWiFS: A preliminary algorithm. Appl Opt 33:443-452

Gordon HR, Wang M (1994b) Influence of oceanic whitecaps on atmospheric correction of ocean-color sensors. Appl Opt 33:7754-7763

Groom SB, Holligan PM (1987) Remote sensing of coccolithophore blooms. Adv Space Res 7:73-78

Holligan, PM, Charalampopoulou A, Hutson R (2010) Seasonal distributions of the coccolithophore, *Emiliania huxleyi*, and of particulate inorganic carbon in surface waters of the Scotia Sea. J Mar Syst 82:195-205

Holligan PM, Viollier M, Harbour DS, Camus P, Champagne-Philippe M (1983) Satellite and ship studies of coccolithophore production along a continental-shelf edge. Nature 304:339-342

Hooker SB, Zibordi G, Lazin G (1999) The SeaBOARR-98 Field Campaign. NASA Tech. Memo. 1999-206892, Vol. 3, Hooker SB, Firestone ER (eds) NASA Goddard Space Flight Center, Greenbelt, Maryland, 40 p

Iglesias-Rodríguez MD, Brown CW, Doney SC, Kleypas J, Kolber D, Kolber Z, Hayes PK, Falkowski PG (2002) Representing key phytoplankton functional groups in ocean carbon cycle models: Coccolithophorids. Global Biogeochem Cycles 16:1100

Johnson BD, Cooke RC (1981) Generation of stabilized microbubbles in seawater. Science 213:209-211

Koepke P (1984) Effective reflectance of oceanic whitecaps. Appl Opt 23:1816-1824

Lee Z, Carder KL, Arnone RA (2002) Deriving inherent optical properties from water color: A multiband quasi-analytical algorithm for optically deep waters. Appl Opt 41:5755-5772

Malin G, Steinke M (2004) Dimethyl sulphide production: What is the contribution of the coccolithophores? In: Thierstein HR, Young JR (eds) Coccolithophores: From molecular processes to global impact. Springer, Berlin p 127-164

Mobley CD (1994) Light and Water: Radiative Transfer in Natural Waters, Academic Press, San Diego

Mobley CD (1999) Estimation of the remote-sensing reflectance from above-surface measurements. Appl Opt 38:7442-7455

Monahan EC, Lu M (1990) Acoustically relevant bubble assemblages and their dependence on meteorological parameters. IEEE J Ocean Eng 15:340-349

Moore KD, Voss KJ, Gordon HR (2000) Spectral reflectance of whitecaps: Their contribution to water-leaving radiance. J Geophys Res-Oceans 105:6493-6499

Moore TS, Dowell MD, Franz BA (2012) Detection of coccolithophore blooms in ocean color satellite imagery: A generalized approach for use with multiple sensors. Remote Sens Environ 117:249-263

Mueller JL (1976) Ocean color spectra measured off Oregon coast: Characteristic vectors. Appl Opt 15:394-402

Mueller JL et al. (2003) Radiometric Measurements and Data Analysis Protocols, Vol. III, Goddard Space Flight Center, Greenbelt, Md, 78 p

O'Reilly JE, Maritorena S, Mitchell BG, Siegel DA, Carder KL, Garver SA, Kahru M, McClain C (1998) Ocean color chlorophyll algorithms for SeaWiFS. J Geophys Res-Oceans 103:24937-24953

Paasche E (2001) A review of the coccolithophorid *Emiliania huxleyi* (Prymnesiophyceae), with particular reference to growth, coccolith formation, and calcification-photosynthesis interactions. Phycologia 40:503-529

Painter SC, Poulton AJ, Allen JT, Pidcock R, Balch WM (2010) The COPAS'08 expedition to the Patagonian Shelf: Physical and environmental conditions during the 2008 coccolithophore bloom. Cont Shelf Res 30:1907-1923

Poulton AJ, Young JR, Bates NR, Balch WM (2011) Biometry of detached *Emiliania huxleyi* coccoliths along the Patagonian Shelf. Mar Ecol Prog Ser 443:1-17

Randolph K, Dierssen H, Twardowski M, Zappa C, Cifuentes-Lorenzen A, Freeman S, Balch W, Drapeau D, Bowler B (2010) Optical measurements of bubble populations during large scale wave breaking in the Southern Ocean and their significance to remote sensing reflectance. Proc. Ocean Optics XX

Randolph K, Dierssen HM, Twardowski M, Cifuentes-Lorenzen A, Zappa CJ (2014), Optical measurements of small deeply penetrating bubble populations generated by breaking waves in the Southern Ocean, J Geophys Res-Oceans 119

Risien CM, Chelton DB (2008) A global climatology of surface wind and wind stress fields from eight years of QuikSCAT scatterometer data. J Phys Oceanogr, 38: 2379-2413

Rost B, Riebesell U (2004) Coccolithophore calcification and the biological pump: Response to environmental changes. In: Thierstein HR, Young JR (eds) Coccolithophores: From molecular processes to global impact. Springer, Berlin p 99-125

Siegel DA, Wang M, Maritorena S, Robinson W (2000) Atmospheric correction of satellite ocean color imagery: The black pixel assumption. Appl Opt 39:3582-3591

Signorini SR, Garcia VMT, Piola AR, Garcia CAE, Mata MM, McClain CR (2006) Seasonal and interannual variability of calcite in the vicinity of the Patagonian shelf break (38°S-52°S). Geophys Res Lett 33:L16610

Smith SR, Bourassa MA, Sharp RJ (1999) Establishing more truth in true winds. J Atmos Ocean Technol 16:939-952

Smith SR, Harvey C, Legler DM (1996) Handbook of Quality control procedures and methods for surface meteorological data, WOCE Report No. 141/96, COAPS Report No. 96-1

Stramski D (1994) Gas microbubbles: An assessment of their significance to light scattering in quiescent seas. Proc. Ocean Optics XII

Stramski D, Tegowski J (2001) Effects of intermittent entrainment of air bubbles by breaking wind waves on ocean reflectance and underwater light field. J Geophys Res 106:31345-31360

Terrill EJ, Melville WK, Stramski D (2001) Bubble entrainment by breaking waves and their influence on optical scattering in the upper ocean. J Geophys Res-Oceans 106:16815-16823

Thorpe SA (1982) On the clouds of bubbles formed by breaking wind-waves in deep water, and their role in air-sea gas transfer. Philos Trans R Soc Lond A 304:155-210

Thorpe SA (1992) Bubble clouds and the dynamics of the upper ocean. Q J R Meteorol Soc 118:1-22

Thorpe SA (1995) Dynamical processes of transfer at the sea surface. Prog Oceanogr 35:315-352

Thuillier G, Hersé, M, Labs D, Foujols T, Peetermans W, Gillotay D, Simon PC, Mandel H (2003) The solar spectral irradiance from 200 to 2400 nm as measured by the SOLSPEC spectrometer from the Atlas and Eureca missions. Sol Phys 214:1-22

Tyrrell T, Holligan PM, Mobley CD (1999) Optical impacts of oceanic coccolithophore blooms. J Geophys Res-Oceans 104:3223-3241

Tyrrell T, Merico A (2004) *Emiliania huxleyi*: Bloom observations and the conditions that induce them. In: Thierstein HR, Young JR (eds) Coccolithophores: From molecular processes to global impact. Springer, Berlin p 75-97

Voss KJ, Balch WM, Kilpatrick KA (1998) Scattering and attenuation properties of *Emiliania huxleyi* cells and their detached coccoliths. Limnol Oceanogr 43:870-876

Wilks DS (2006) Statistical methods in the atmospheric sciences. Elsevier, Amsterdam

Winter A, Jordan RW, Roth PH (1994) Biogeography of living coccolithophores in ocean waters. In: Winter A, Siesser WG (eds) Coccolithophores, p 161-177

Yan B, Chen B, Stamnes K (2002) Role of oceanic air bubbles in atmospheric correction of ocean color imagery. Appl Opt 41:2202-2212

Zhang X (2001) Influence of bubbles on the water-leaving reflectance. PhD Thesis, Dalhousie University, Halifax

Zhang X, Lewis M, Bissett WP, Johnson B, Kohler D (2004) Optical influence of ship wakes. Appl Opt 43:3122-3132

Zhang X, Lewis M, Johnson B (1998) Influence of bubbles on scattering of light in the ocean. Appl Opt 37:6525-6536

Zhang X, Lewis M, Lee M, Johnson B, Korotaev G (2002) The volume scattering function of natural bubble populations. Limnol Oceanogr 47:1273-1282